Supplementary information: Thermal Transport in Ag_8TS_6 (T= Si, Ge, Sn) Argyrodites: An Integrated Experimental, Quantum-Chemical, and Computational Modelling Study

*Joana Bustamante,[a] Anupama Ghata,[b] Aakash A. Naik, [a,c] Christina Ertural,[a] Katharina Ueltzen,[a,c] Wolfgang G. Zeier,[b,d] and Janine George *[a,c]*

[a]Federal Institute for Materials, Research and Testing, Department Materials Chemistry, Unter den Eichen 87, 12205 Berlin, Germany.

[b]University of Münster, Institute of Inorganic and Analytical Chemistry, Corrensstr. 28/30, D-48149 Münster, Germany.

[c]Friedrich Schiller University Jena, Institute of Condensed Matter Theory and Solid-State Optics, Max-Wien-Platz 1, 07743 Jena, Germany.

[d]Institute of Energy Materials and Devices (IMD), IMD-4: Helmholtz-Institut Muenster, Forschungszentrum Jülich, 48149 Münster, Germany.

E-mail: janine.george@bam.de

Content

Section S1: Phase analysis and Rietveld refinements of Ag_8TS_6 (T = Si, Ge, Sn)

Rietveld refinements were performed at all temperature steps for all three compositions of Ag_8TS_6 (T = Si, Ge, Sn) using the Topas-Academic V7 software package.[1] A Chebyshev polynomial function was used to model the background, whereas the peak shapes were described using a modified Thompson-Cox-Hastings pseudo-Voigt function.[2] At first, refinements were carried out for background coefficients, sample displacement, lattice parameters, and peak shapes. After that, the fractional atomic coordinates and the isotropic thermal displacement parameters of atoms were refined. The refinements proceeded sequentially, starting with sulfur (S^{2-}), moving to T^{4+} (T = Si, Ge, Sn), and finally silver (Ag^{+}). To reduce the number of free variables in the refinements, the isotropic thermal displacement parameters for all silver (Ag^{+}) atoms were constrained to be equal across all three compositions. Similarly, the isotropic thermal displacement parameter for T^{4+} (T = Si, Ge, Sn) atoms and all sulfur atoms (S^{2-}) were also considered to be equal for better refinement quality.

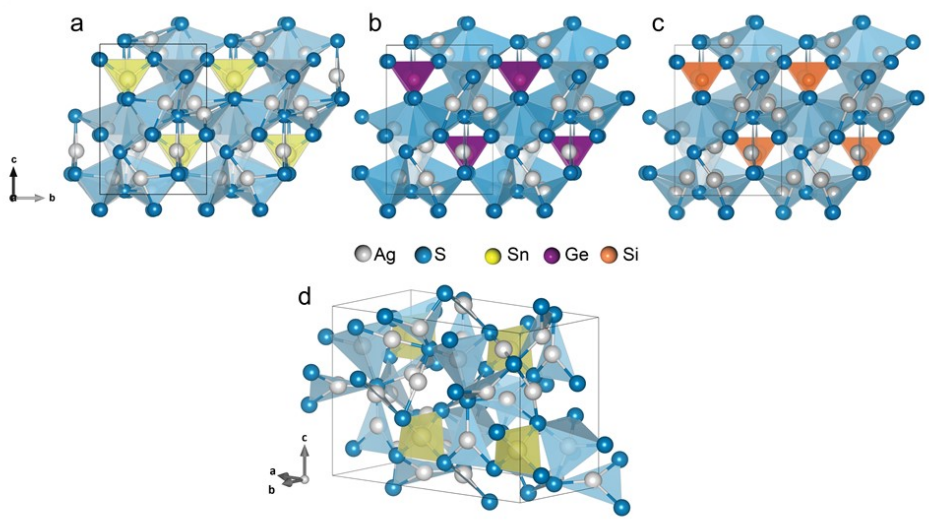

Figure S1*.a-c) Representation of Ag_8SiS_6, Ag_8GeS_6, and Ag_8SnS_6 argyrodites in the orthorhombic $Pna2_1$ phase at room temperature, respectively. d) Alternative view of the RT-Ag_8SnS_6 argyrodites showing the Ag—Ag connectivity and the diversity of the Ag environments.*

The results of Rietveld refinements of Ag_8TS_6 (T = Si, Ge, Sn) at 298 K are presented in **Tables S1-S3**, and **Figure S2**, while the X-ray diffraction patterns at all measured temperatures are shown in **Figure S3**. The refined lattice parameters and unit cell volume for all compositions are also tabulated (**Table S4-S6**). From the slope of the unit cell volume vs. temperature plots (**Figure S4**), the thermal volume expansion coefficients were calculated for each composition. The R_{wp} and the goodness-of-fit (GoF) value indicate the refinement quality.

Table S1. *Structural parameters of Ag_8SiS_6 at 298 K as obtained by Rietveld refinements and utilizing laboratory X-ray diffraction (Mo Kα radiation).*

Structural information of Ag_8SiS_6 from X-ray diffraction data at 298 K Space group: $Pna2_1$; λ (Mo Kα) = 0.7093Å; Lattice parameters: *a* = 15.058 (1) Å, *b* = 7.4355(6) Å, *c* = 10.5415(9) Å, R_{wp} = 7.81%; GoF = 2.11						
Atom	**Wyckoff site**	***x***	***Y***	***z***	**Occ.**	**B_{eq} / Å²**
Ag1	4*a*	0.01681(5)	0.011(1)	0.016(1)	1	3.53(9)
Ag2	4*a*	0.0640(4)	0.2287(8)	0.255(1)	1	3.53(9)
Ag3	4*a*	0.1244(4)	0.2236(8)	0.787(6)	1	3.53(9)
Ag4	4*a*	0.2206(5)	-0.006(1)	-0.006(1)	1	3.53(9)
Ag5	4*a*	0.2607(4)	0.114(1)	0.305(2)	1	3.53(9)
Ag6	4*a*	0.2690(5)	0.380(1)	0.091(1)	1	3.53(9)
Ag7	4*a*	0.4194(5)	0.098(1)	0.107(1)	1	3.53(9)
Ag8	4*a*	0.4327(6)	0.068(1)	0.436(1)	1	3.53(9)
Si	4*a*	0.133(1)	0.750(3)	0.241(2)	1	0.07(1)
S1	4*a*	-0.019(1)	0.281(3)	0.644(2)	1	0.07(1)
S2	4*a*	0.126(1)	0.286(2)	0.025(2)	1	0.07(1)
S3	4*a*	0.126(1)	0.492(3)	0.380(2)	1	0.07(1)
S4	4*a*	0.266(1)	0.229(2)	0.644(2)	1	0.07(1)
S5	4*a*	0.378(1)	0.325(2)	0.291(3)	1	0.07(1)
S6	4*a*	0.625(1)	0.551(2)	0.390(2)	1	0.07(1)

Table S2. *Structural parameters of Ag_8GeS_6 at 298 K as obtained by Rietveld refinements and utilizing laboratory X-ray diffraction (Mo Kα radiation). Results for this structure have been previously reported by Ghata et al.* [3]

Structural information of Ag_8GeS_6 from X-ray diffraction data at 298 K Space group: $Pna2_1$; λ (Mo Kα) = 0.7093Å; Lattice parameters: *a* = 15.147(1) Å, *b* = 7.4695(5) Å, *c* = 10.5852(7) Å, R_{wp} = 4.78%; GoF = 1.49						
Atom	**Wyckoff site**	***x***	***Y***	***z***	**Occ.**	**B_{eq} / Å²**
Ag1	4*a*	0.0170(3)	0.0082(9)	0.0172(6)	1	3.39(6)
Ag2	4*a*	0.0625(3)	0.2250(6)	0.2556(5)	1	3.39(6)
Ag3	4*a*	0.1247(3)	0.2239(6)	0.7940(6)	1	3.39(6)
Ag4	4*a*	0.2234(3)	-0.0007(7)	-0.0019(5)	1	3.39(6)
Ag5	4*a*	0.2605(3)	0.1251(7)	0.3209(5)	1	3.39(6)
Ag6	4*a*	0.2731(3)	0.3800(6)	0.0990(4)	1	3.39(6)
Ag7	4*a*	0.4154(5)	0.0997(9)	0.1194(8)	1	3.39(6)

Ag8	4*a*	0.4351(4)	0.0649(7)	0.4350(4)	1	3.39(6)
Ge	4*a*	0.1247(3)	0.7301(7)	0.2664(7)	1	0.48(7)
S1	4*a*	-0.007(1)	0.271(2)	0.643(1)	1	0.48(7)
S2	4*a*	0.1218(9)	0.268(1)	0.027(1)	1	0.48(7)
S3	4*a*	0.128(1)	0.471(1)	0.392(1)	1	0.48(7)
S4	4*a*	0.257(1)	0.231(1)	0.638(1)	1	0.48(7)
S5	4*a*	0.3870(9)	0.323(1)	0.299(1)	1	0.48(7)
S6	4*a*	0.631(1)	0.519(1)	0.400(1)	1	0.48(7)

Table S3. *Structural parameters of Ag_8SnS_6 at 298 K as obtained by Rietveld refinements and utilizing laboratory X-ray diffraction (Mo Kα radiation).*

Structural information of Ag_8SnS_6 from X-ray diffraction data at 298 K Space group: $Pna2_1$; λ (Mo Kα) = 0.7093Å; Lattice parameters: *a* = 15.3119(7) Å, *b* = 7.5542(5) Å, *c* = 10.7071(5) Å, R_{wp} = 5.36%; GoF = 1.23						
Atom	**Wyckoff site**	***x***	***Y***	***z***	**Occ.**	**B_{eq} / Å²**
Ag1	4*a*	0.0198(3)	0.1463(9)	0.0165(6)	1	3.55(6)
Ag2	4*a*	0.0617(3)	0.2273(6)	0.2533(8)	1	3.55(6)
Ag3	4*a*	0.1233(3)	0.2201(7)	0.8024(9)	1	3.55(6)
Ag4	4*a*	0.2224(3)	0.0096(7)	0.0056(9)	1	3.55(6)
Ag5	4*a*	0.2576(4)	0.1562(7)	0.3465(8)	1	3.55(6)
Ag6	4*a*	0.2768(3)	0.3779(6)	0.1041(8)	1	3.55(6)
Ag7	4*a*	0.4112(3)	0.0797(7)	0.1243(8)	1	3.55(6)
Ag8	4*a*	0.4366(4)	0.0627(7)	0.4334(8)	1	3.55(6)
Sn	4*a*	0.1254(2)	0.7312(5)	0.2699(8)	1	0.63(5)
S1	4*a*	0.002(1)	0.266(2)	0.639(1)	1	0.63(5)
S2	4*a*	0.1257(9)	0.278(1)	0.033(1)	1	0.63(5)
S3	4*a*	0.127(1)	0.476(1)	0.397(1)	1	0.63(5)
S4	4*a*	0.247(1)	0.229(1)	0.629(1)	1	0.63(5)
S5	4*a*	0.3897(9)	0.323(1)	0.296(1)	1	0.63(5)
S6	4*a*	0.631(1)	0.516(1)	0.408(1)	1	0.63(5)

Table S4. *Temperature-dependent variations in lattice parameters and unit-cell volumes of Ag_8SiS_6 from 100 K to 400 K based on Rietveld refinements.*

Temperature / K	**Space group**	**Lattice parameters / Å**	**Unit cell volume / Å³**
103	$Pna2_1$	a = 15.009(1) b = 7.4122(7)	1167.7(2)

		c = 10.495(1)	
123	$Pna2_1$	a = 15.016(1) b = 7.4155(6) c = 10.5019(9)	1169.4(1)
133	$Pna2_1$	a = 15.019(1) b = 7.4173(7) c = 10.5038(8)	1170.2(1)
153	$Pna2_1$	a = 15.022(1) b = 7.4184(7) c = 10.508(1)	1171.0(2)
173	$Pna2_1$	a = 15.029(1) b = 7.4218(6) c = 10.5153(8)	1172.9(1)
193	$Pna2_1$	a = 15.031(1) b = 7.4240(9) c = 10.517(1)	1173.6(2)
213	$Pna2_1$	a = 15.034(1) b = 7.4252(7) c = 10.521(1)	1174.6(2)
233	$Pna2_1$	a = 15.041(1) b = 7.4279(7) c = 10.526(1)	1176.1(2)
253	$Pna2_1$	a = 15.050(1) b = 7.4320(7) c = 10.533(1)	1178.2(1)
273	$Pna2_1$	a = 15.053(1) b = 7.4346(7) c = 10.536(1)	1179.2(2)
293	$Pna2_1$	a = 15.058(1) b = 7.4355(9) c = 10.539(1)	1180.1(2)
313	$Pna2_1$	a = 15.062(1) b = 7.4376(8) c = 10.544(1)	1181.2(2)
333	$Pna2_1$	a = 15.072(1) b = 7.4422(8)	1183.4(2)

		c = 10.550(1)	
353	$Pna2_1$	a = 15.078(1) b = 7.4448(9) c = 10.555(1)	1184.9(2)
373	$Pna2_1$	a = 15.084(1) b = 7.4493(8) c = 10.561(1)	1186.7(2)
400	$Pna2_1$	a = 15.092(1) b = 7.4524(8) c = 10.566(1)	1188.5(2)

Table S5. *Temperature-dependent variations in lattice parameters and unit-cell volumes of Ag_8GeS_6 from 100 K to 400 K based on Rietveld refinements.*

Temperature / K	**Space group**	**Lattice parameters / Å**	**Unit cell volume / Å^3**
103	$Pna2_1$	a = 15.110(1) b = 7.4477(5) c = 10.5483(8)	1187.1(1)
123	$Pna2_1$	a = 15.111(1) b = 7.4478(6) c = 10.5494(8)	1187.2(1)
133	$Pna2_1$	a = 15.110(1) b = 7.4480(5) c = 10.5493(7)	1187.3(1)
153	$Pna2_1$	a = 15.115(1) b = 7.4502(6) c = 10.5544(9)	1188.6(1)
173	$Pna2_1$	a = 15.119(1) b = 7.4536(6) c = 10.5582(9)	1189.8(1)
193	$Pna2_1$	a = 15.122(1) b = 7.4547(6) c = 10.5628(9)	1190.7(1)
213	$Pna2_1$	a = 15.129(1) b = 7.4587(7)	1192.4(1)

		c = 10.567(1)	
233	$Pna2_1$	a = 15.133(1) b = 7.4607(7) c = 10.571(1)	1193.6(1)
253	$Pna2_1$	a = 15.136(1) b = 7.4656(7) c = 10.5797(9)	1194.5(1)
273	$Pna2_1$	a = 15.141(1) b = 7.4376(8) c = 10.544(1)	1195.9(1)
298	$Pna2_1$	a = 15.147(1) b = 7.4695(5) c = 10.5852(7)	1197.7(1)
313	$Pna2_1$	a = 15.152(1) b = 7.4718(8) c = 10.588(1)	1198.8(2)
333	$Pna2_1$	a = 15.157(2) b = 7.474(1) c = 10.593(1)	1200.0(3)
353	$Pna2_1$	a = 15.162(1) b = 7.4783(8) c = 10.598(1)	1201.8(2)
373	$Pna2_1$	a = 15.169(1) b = 7.4815(8) c = 10.603(1)	1203.3(2)
400	$Pna2_1$	a = 15.169(2) b = 7.483(1) c = 10.606(1)	1204.1(9)

Table S6. *Temperature-dependent variations in lattice parameters and unit-cell volumes of Ag_8SnS_6 from 100 K to 400 K based on Rietveld refinements.*

Temperature / K	**Space group**	**Lattice parameters / Å**	**Unit cell volume / Å^3**
103	$Pna2_1$	a = 15.2835 (6) b = 7.5221(3) c = 10.6698(4)	1226.66(9)

123	$Pna2_1$	a = 15.2855(6) b = 7.5248(3) c = 10.6727(4)	1227.59(9)
133	$Pna2_1$	a = 15.2860(6) b = 7.5253(3) c = 10.6738(4)	1227.83(9)
153	$Pna2_1$	a = 15.2876(9) b = 7.5282(4) c = 10.6765(4)	1228.7(1)
173	$Pna2_1$	a = 15.2889(9) b = 7.5305(4) c = 10.6793(6)	1229.5(1)
193	$Pna2_1$	a = 15.292(9) b = 7.5344(6) c = 10.6838(9)	1231.0(1)
213	$Pna2_1$	a = 15.296(2) b = 7.5389(5) c = 10.6884(7)	1232.5(1)
233	$Pna2_1$	a = 15.299(1) b = 7.5423(5) c = 10.6928(7)	1233.9(1)
253	$Pna2_1$	a = 15.304(1) b = 7.5467(5) c = 10.6986(7)	1235.6(1)
273	$Pna2_1$	a = 15.3103(8) b = 7.5510(4) c = 10.7034(6)	1237.4(1)
293	$Pna2_1$	a = 15.311(1) b = 7.5534(8) c = 10.706(1)	1238.2(2)
313	$Pna2_1$	a = 15.317(1) b = 7.5586(1) c = 10.7134(1)	1240.4(1)
333	$Pna2_1$	a = 15.322(1) b = 7.5625(6) c = 10.7174(9)	1241.8(1)

353	$Pna2_1$	a = 15.325(1) b = 7.5661(7) c = 10.7228(9)	1243.3(1)
373	$Pna2_1$	a = 15.328(1) b = 7.5696(9) c = 10.726(1)	1244.5(2)
400	$Pna2_1$	a = 15.332(2) b = 7.575(1) c = 10.733(1)	1246.6(3)

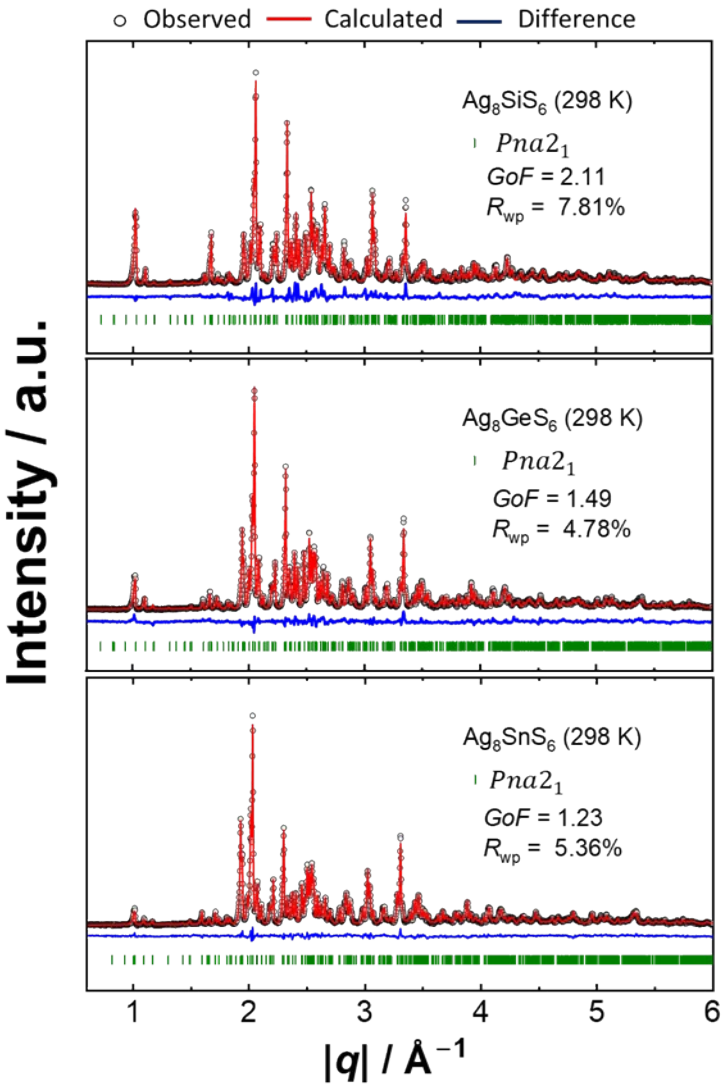

Figure S2. *X-ray diffraction patterns and corresponding Rietveld refinement results of Ag_8TS_6 (T = Si, Ge, Sn) at 298 K.*

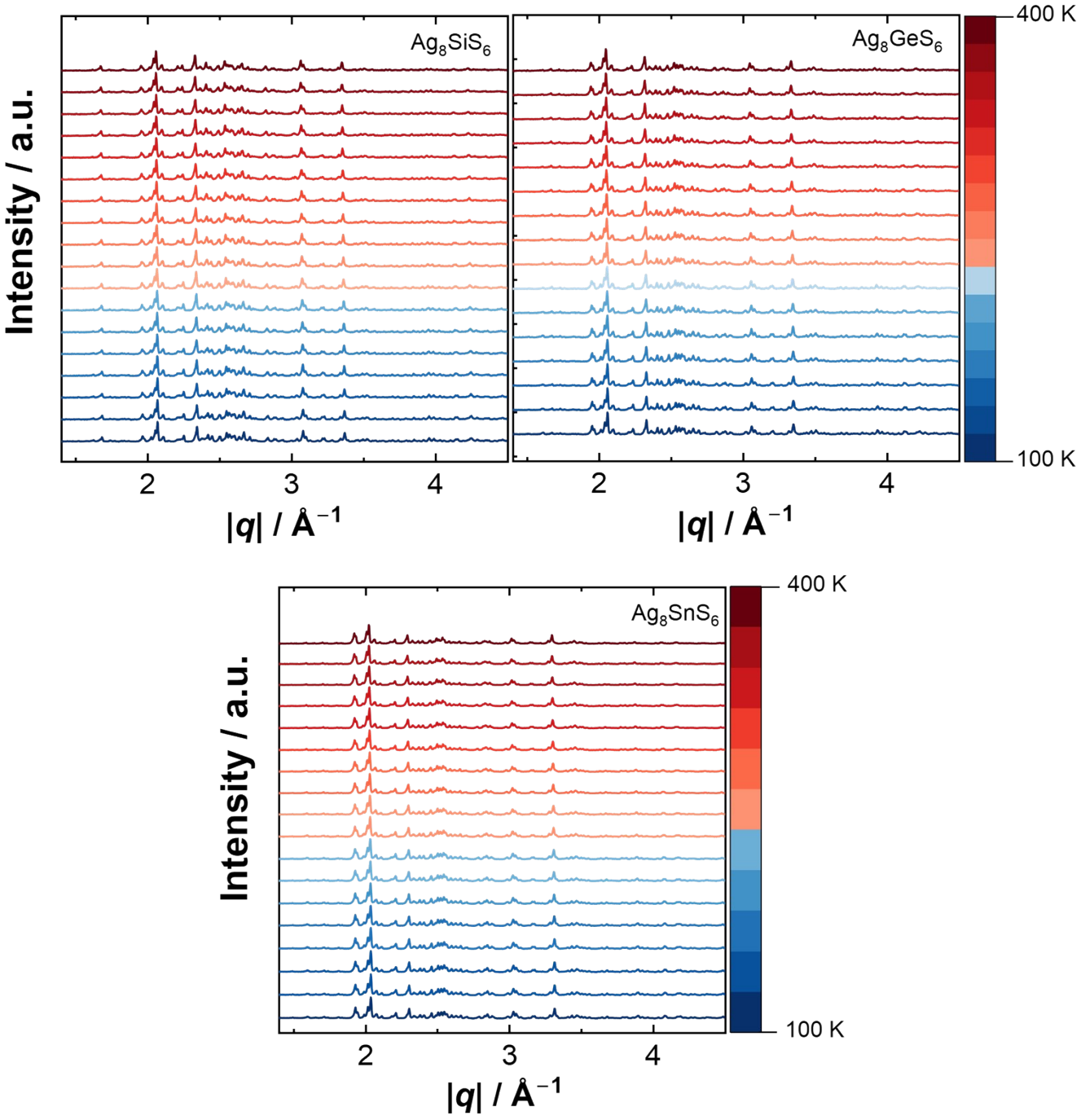

Figure S3. *Temperature-dependent X-ray diffraction patterns of Ag_8TS_6 (T = Si, Ge, Sn) measured over the temperature range of 100 K to 400 K.*

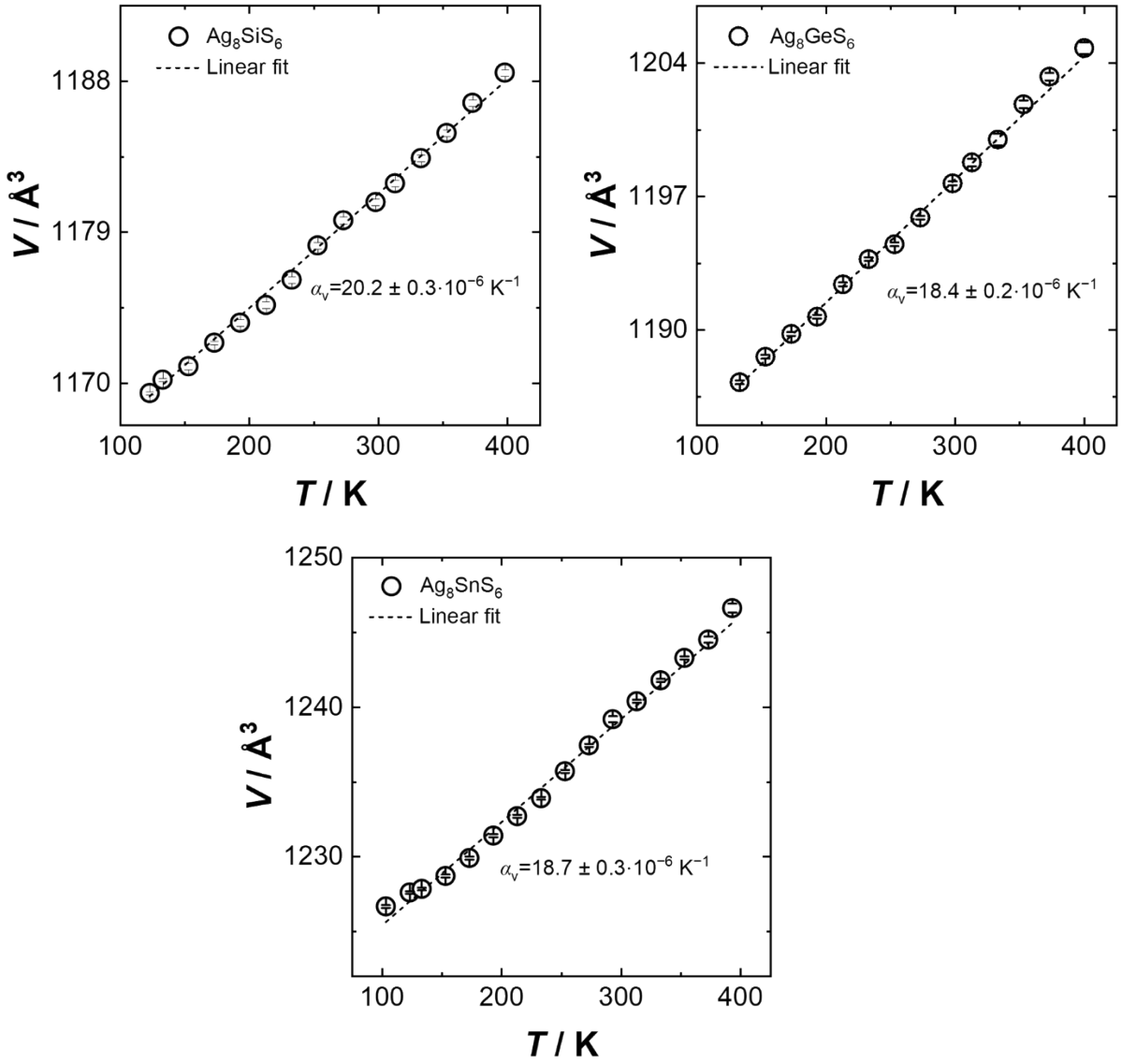

Figure S4. *Unit cell volume change of Ag_8TS_6 (T = Si, Ge, Sn) with temperature; the thermal volume expansion coefficient can be determined from the slopes of the plots.*

Section S2: Computational details – Stability and Bonding analysis

Computed lattice parameters *a*, *b*, and *c* for all the structures presented in **Figure S1** are reported in **Table S7**. Here, our computed lattice parameters show only ~2% overestimation with respect to experimental values, which lies within the typical error range of DFT calculations and ensures the robustness of our computational approach. In addition, a slight decrease in the volume is observed when we move from Sn to Ge and Si, consistent with the expected trend of decreasing atomic radii from bottom to top within the groups.

Table S7. *Computational lattice parameters for Ag_8TS_6 (T = Si, Ge, and Sn) compared with experimental measurements obtained by Rietveld refinements at 298 K*

Unit cell	**Ag_8SiS_6**		**Ag_8GeS_6**		**Ag_8SnS_6 (RT)**		**Ag_8SnS_6 (LT)**	
		Exp*		Exp*		Exp*		Exp**
a (Å)	15.16	15.058	15.27	15.147	15.46	15.3119	7.78	7.66
b (Å)	7.59	7.4355	7.62	7.4695	7.70	7.5542	7.67	7.54
c (Å)	10.69	10.5415	10.72	10.5852	10.85	10.7071	10.86	10.63
V ($Å^3$)	1228.61	1180.266	1246.84	1197.615	1291.25	1238.481	648.10	614.15
V/Z ($Å^3$)	307.15	295.0665	311.71	299.404	322.81	309.6203	324.05	307.08

*Our Experimental values **Experimental data from Slade's work [4]

Based on the optimised structures, we analysed the material's stability with harmonic phonon calculations. The phonon band structures of all studied argyrodites do not show any imaginary modes, confirming their dynamical stability. We believe that the LO-TO splitting at the Γ-point, evident in **Figure 3** and **Figures S5,** arises from the ionic character of the compounds and the inclusion of the non-analytical term correction.

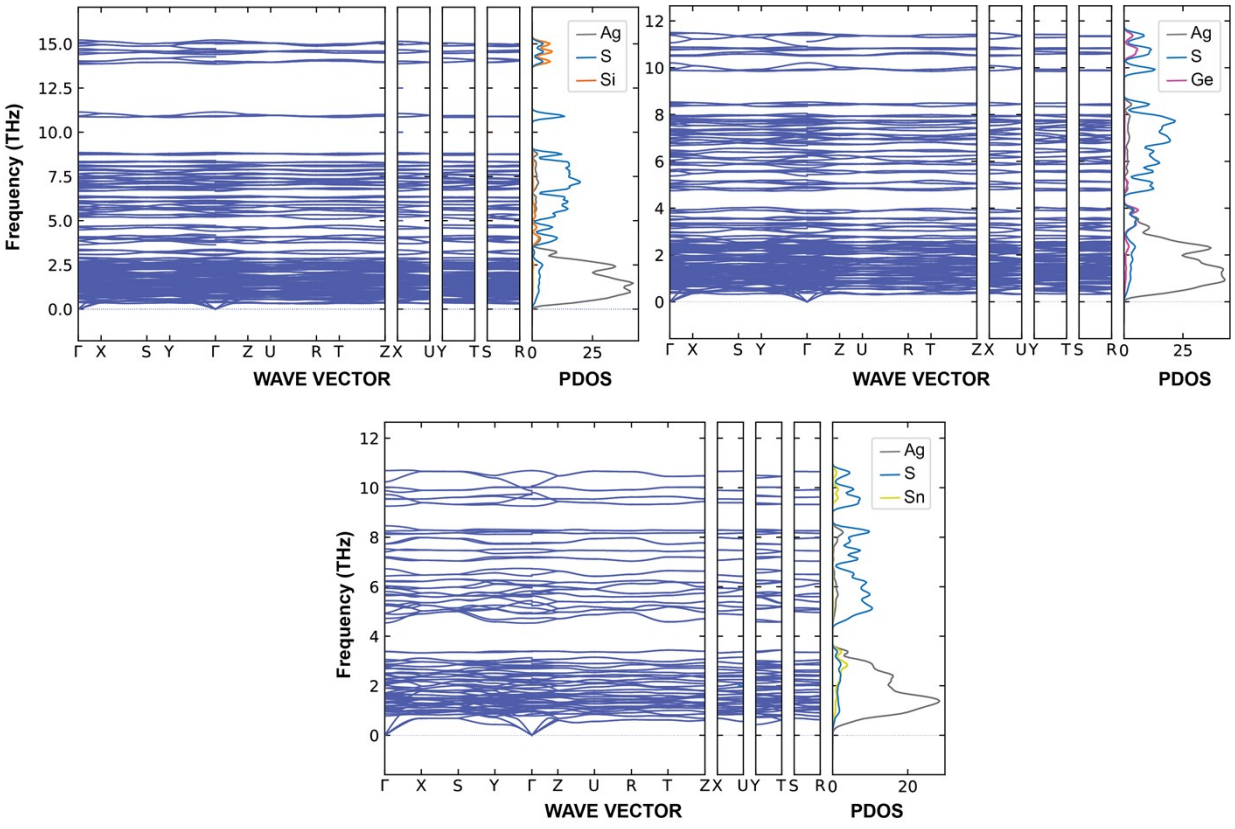

Figure S5. *Phonon dispersion curves for the Ag_8SiS_6, Ag_8GeS_6, and low-temperature phase of Ag_8SnS_6 canfieldite.*

Bonding analysis

From our automated bonding analysis, we present coordination environments, Wyckoff positions, ICOHPs, and two-centre ICOBIs per bond for all our argyrodite compounds Ag_8TS_6 (*T*= Si, Ge, and Sn at room and low temperature) in **Figures S6-S9**. We considered ICOHPs and ICOBIs for Ag–Ag bonds less than 3Å.

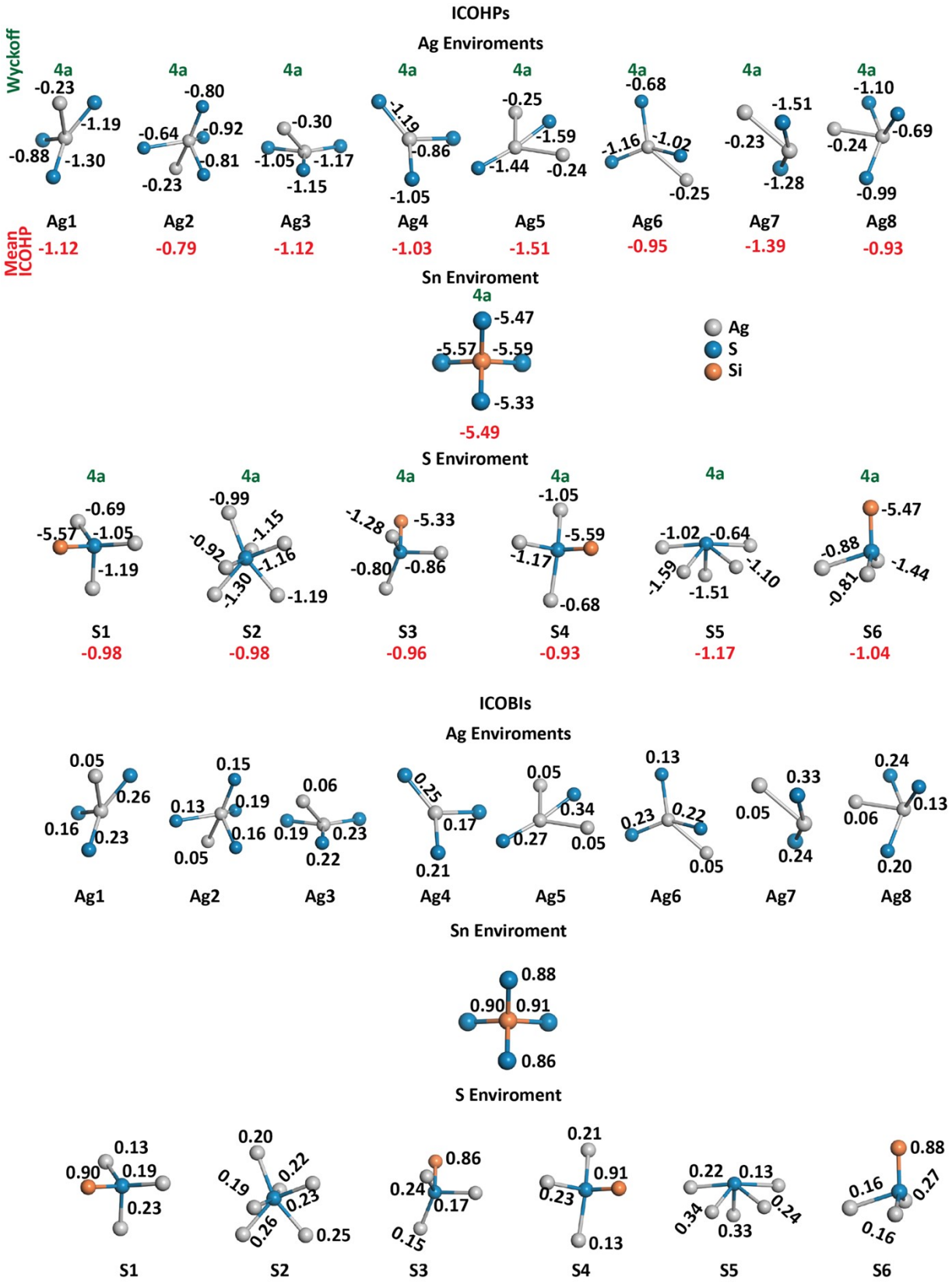

Figure S6. *Local coordination environments, including ICOHPs and ICOBIs per bond for the* Ag_8SiS_6 *structure.*

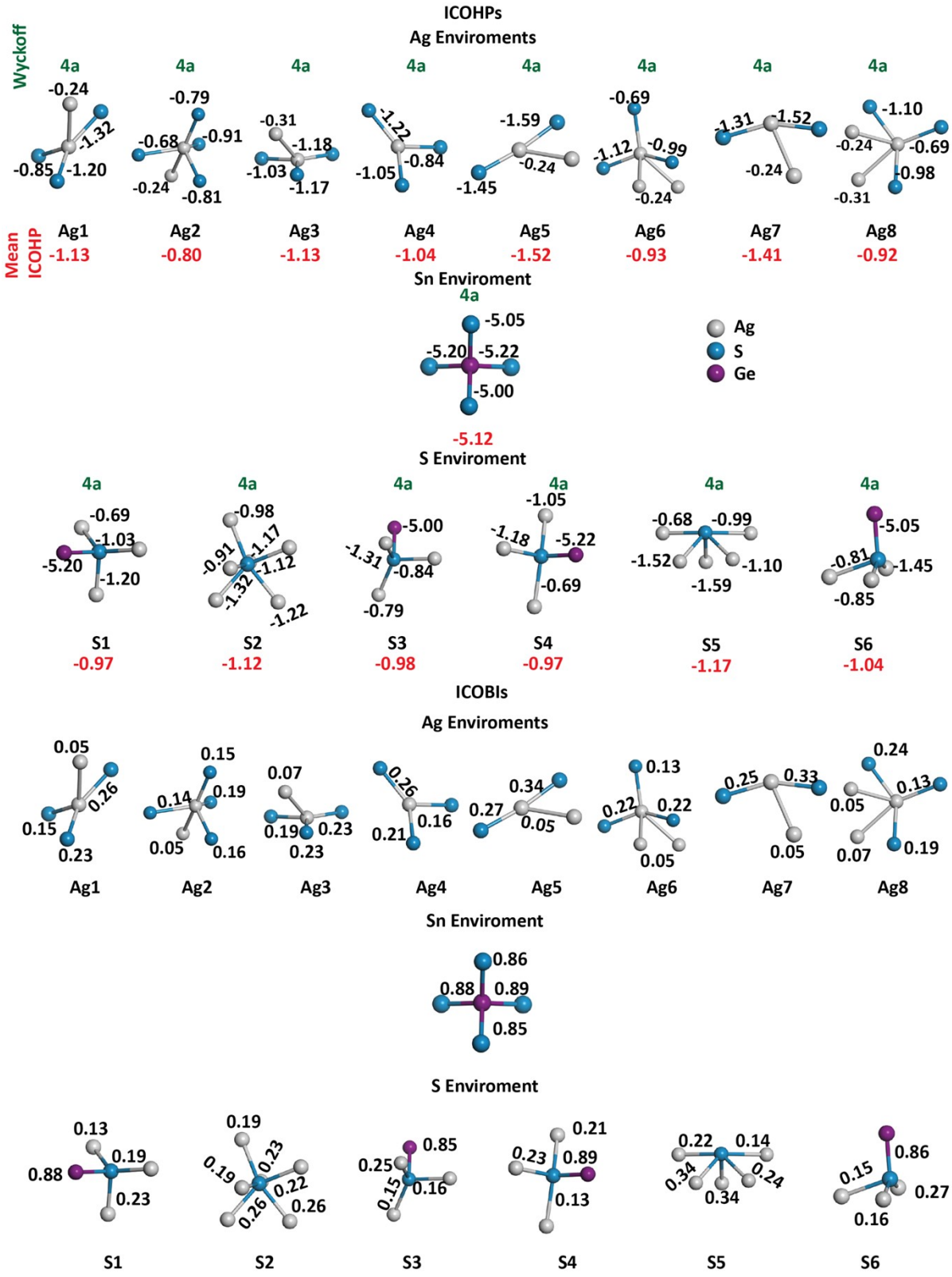

Figure S7*. Local coordination environments, including ICOHPs and ICOBIs per bond for the* Ag_8GeS_6 *structure.*

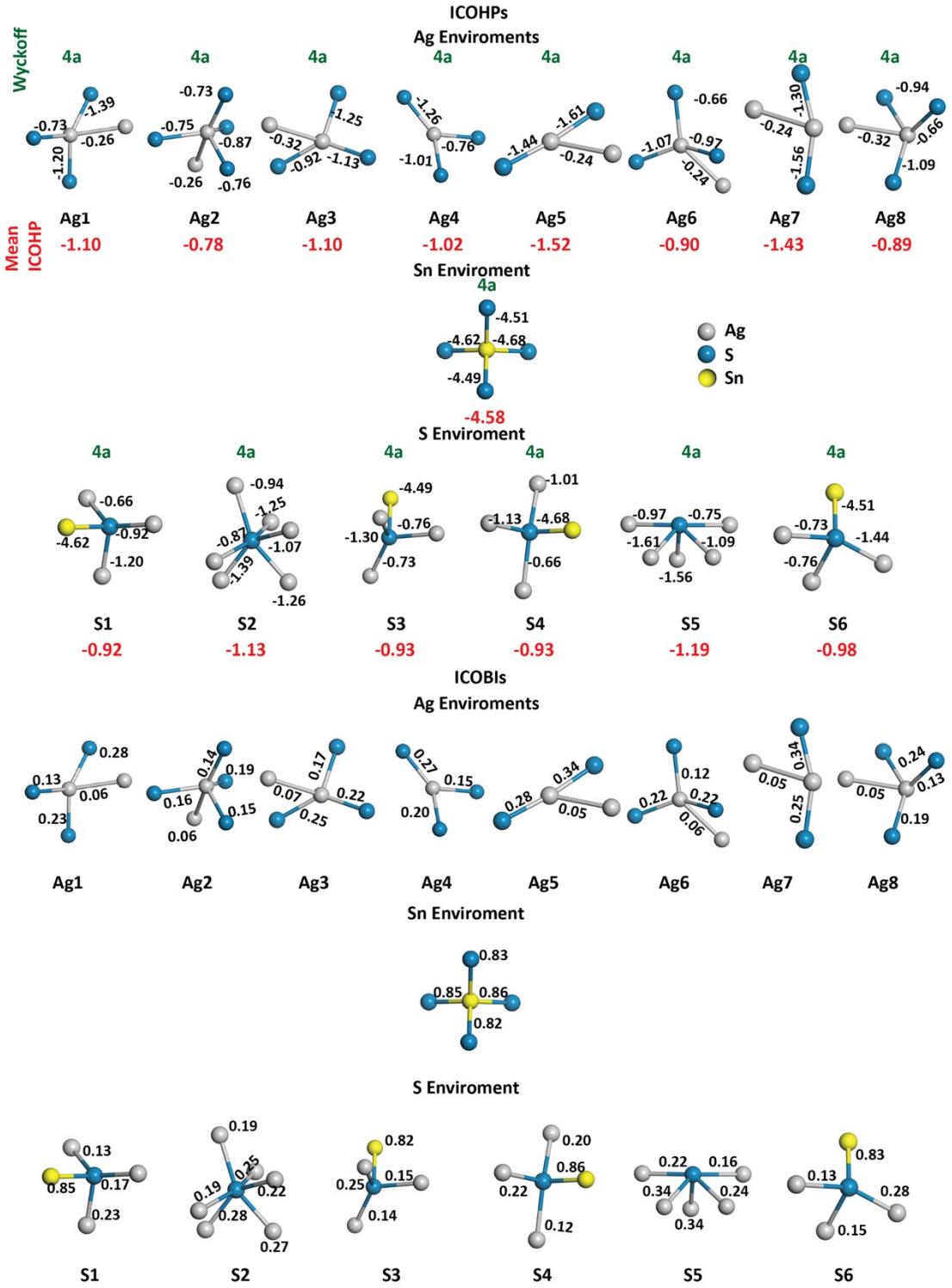

Figure S8. *Local coordination environments, including ICOHPs and ICOBIs per bond for the canfieldite* Ag_8SnS_6 *at room temperature.*

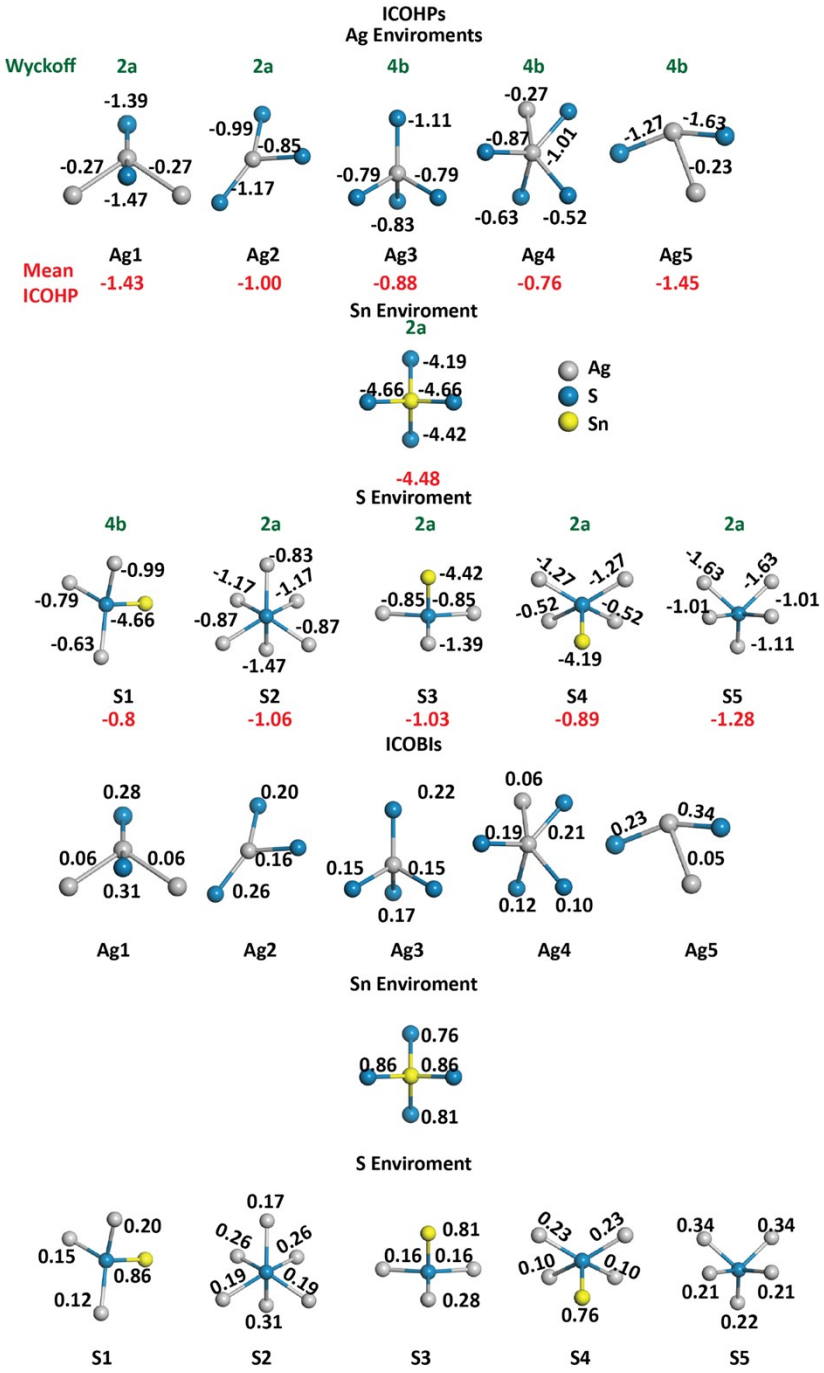

Figure S9. *Local coordination environments, including ICOHPs and ICOBIs per bond for the low-temperature* Ag_8SnS_6.

Table S8. *Atomic positions and inequivalent site fractional coordinates for (*$Pna2_1$*)* Ag_8SiS_6.

Atom	POSCAR Position	Wyckoff Positions	x	y	z	Coordination Environment
Ag1	Ag5	4a	0.014	0.021	0.032	Trigonal Planar
Ag2	Ag9	4a	0.066	0.242	0.252	Tetrahedral
Ag3	Ag13	4a	0.129	0.284	0.783	Trigonal Planar
Ag4	Ag17	4a	0.228	0.007	0.009	Trigonal Planar
Ag5	Ag21	4a	0.261	0.125	0.329	Linear
Ag6	Ag25	4a	0.262	0.383	0.122	Trigonal Planar

Ag7	Ag29	4a	0.410	0.130	0.102	Linear
Ag8	Ag33	4a	0.436	0.071	0.440	Triangular Non-coplanar
Si	Si1	4a	0.123	0.742	0.267	Tetrahedral
S1	S37	4a	0.991	0.266	0.648	Tetrahedral
S2	S41	4a	0.123	0.268	0.019	Trigonal Prismatic
S2	S45	4a	0.120	0.513	0.388	Tetrahedral
S4	S49	4a	0.263	0.232	0.649	Tetrahedral
S5	S53	4a	0.387	0.316	0.287	Square Pyramidal
S6	S57	4a	0.625	0.527	0.385	See-saw like

Table S9. *Atomic positions and inequivalent site fractional coordinates for ($Pna2_1$) Ag_8GeS_6*

Atom	POSCAR Position	Wyckoff Positions	x	y	z	Coordination Environment
Ag1	Ag1	4a	0.015	0.022	0.033	Trigonal Planar
Ag2	Ag5	4a	0.064	0.24	0.252	Tetrahedral
Ag3	Ag9	4a	0.129	0.282	0.785	Trigonal Planar
Ag4	Ag13	4a	0.228	0.009	0.011	Trigonal Planar
Ag5	Ag17	4a	0.261	0.130	0.329	Linear
Ag6	Ag21	4a	0.266	0.382	0.117	Trigonal Planar
Ag7	Ag25	4a	0.409	0.124	0.104	Linear
Ag8	Ag29	4a	0.436	0.07	0.439	Triangular Non-coplanar
Ge	Ge33	4a	0.124	0.740	0.267	Tetrahedral
S1	S37	4a	0.995	0.266	0.643	Tetrahedral
S2	S41	4a	0.123	0.269	0.021	Trigonal Prismatic
S3	S45	4a	0.120	0.503	0.393	Tetrahedral
S4	S49	4a	0.258	0.23	0.644	Tetrahedral
S5	S53	4a	0.387	0.315	0.286	Square Pyramidal
S6	S57	4a	0.626	0.52	0.39	See-saw like

Table S10. *Atomic positions and inequivalent site fractional coordinates for ($Pna2_1$) Ag_8SnS_6*

Atom	POSCAR Position	Wyckoff Positions	x	y	z	Coordination Environment
Ag1	Ag1	4a	0.021	0.022	0.033	Trigonal Planar
Ag2	Ag5	4a	0.060	0.239	0.251	Tetrahedral
Ag3	Ag9	4a	0.129	0.279	0.789	Trigonal Planar
Ag4	Ag13	4a	0.227	0.013	0.016	Trigonal Planar
Ag5	Ag17	4a	0.261	0.138	0.332	Linear
Ag6	Ag21	4a	0.270	0.380	0.111	Triangular Non-coplanar
Ag7	Ag25	4a	0.408	0.114	0.108	Linear
Ag8	Ag29	4a	0.436	0.069	0.436	Triangular Non-coplanar
Sn	Sn33	4a	0.125	0.739	0.266	Tetrahedral
S1	S37	4a	0.001	0.267	0.634	Tetrahedral
S2	S41	4a	0.124	0.27	0.022	Trigonal Prismatic
S3	S45	4a	0.121	0.488	0.4	Tetrahedral
S4	S49	4a	0.249	0.228	0.636	Tetrahedral
S5	S53	4a	0.387	0.310	0.283	Square Pyramidal
S6	S57	4a	0.626	0.506	0.396	See-saw like

Table S11. *Atomic positions and inequivalent site fractional coordinates for LT ($Pmn2_1$) Ag_8SnS_6*

Atom	POSCAR Position	Wyckoff Positions	x	y	z	Coordination Environment
Ag1	Ag1	2a	0	0.313	0.186	Linear
Ag2	Ag3	2a	0.202	0.485	0.389	Trigonal Planar
Ag3	Ag7	4b	0	0.385	0.620	Tetrahedral
Ag4	Ag9	4b	0.292	0.113	0.287	Tetrahedral
Ag5	Ag13	4b	0.273	0.153	0.014	Linear
Sn	Sn17	2a	0	0.754	0.133	Tetrahedral
S1	S19	4b	0.242	0.24	0.757	Tetrahedral
S2	S23	2a	0	0.217	0.401	Octahedral
S3	S25	2a	0	0.497	0.002	Tetrahedral
S4	S27	2a	0	0.989	0.982	Square Pyramidal
S5	S29	2a	0	0.720	0.640	Square Pyramidal

Multi-center bonding analysis

The (Integrated) Crystal Orbital Bond Index (ICOBI) in LOBSTER[5,6] can be a valuable tool to analyze unusual bonding phenomena, as the two-center ICOBI corresponds to the bond order (BO)[6]. Plotting the two-center ICOBI against the bond length leads to the following outcome in **Figure S10**.

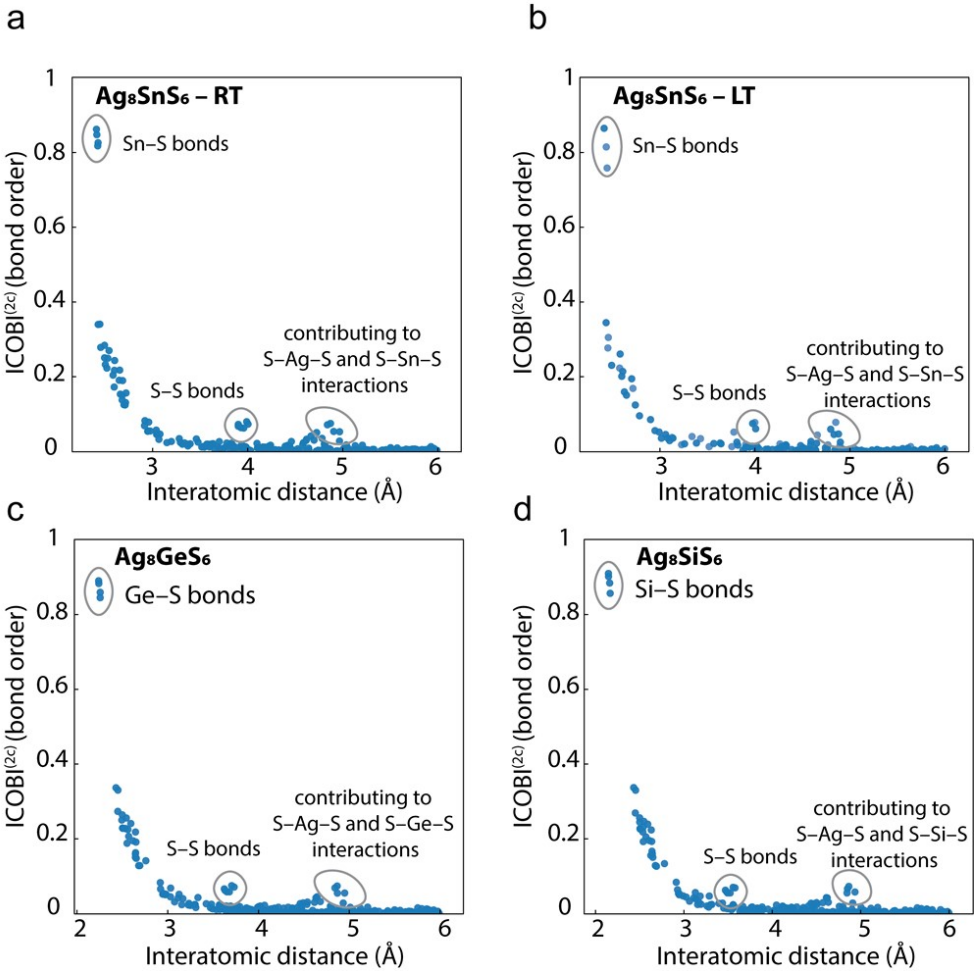

***Figure S10**. Two-center ICOBI vs Interatomic distance plot of Ag_8TS_6 (T = Sn, Ge, Si).*

All phases of Ag_8SnS_6, Ag_8GeS_6, and Ag_8SiS_6 exhibit TS_4 tetrahedra with an ICOBI (or BO) of almost one for each *T*S bond. These tetrahedra also show stronger S—S bonds. They form the covalent backbone of the structures. Then again, all four compounds display a bunch of unusually strong bonds in the range of 4.5 to 5.5 Å, which are suspected of contributing to multi-center interactions.

All atoms with significant three-center bonds formed by two consecutive bonds with significant $ICOBI^{(2c)}$ are shown in the structure inset of **Figure S11**. **Figure S11** shows a more detailed picture of the three-center interactions. Here, the $ICOBI^{(3c)}$ is plotted against the bond angle of S with Ag, Sn, Ge, or Si. Plotting the $ICOBI^{(3c)}$ against the bond angle (**Figure S11**) and the distance of the terminating atoms (**Figure S12**) reveals almost the same correlation.

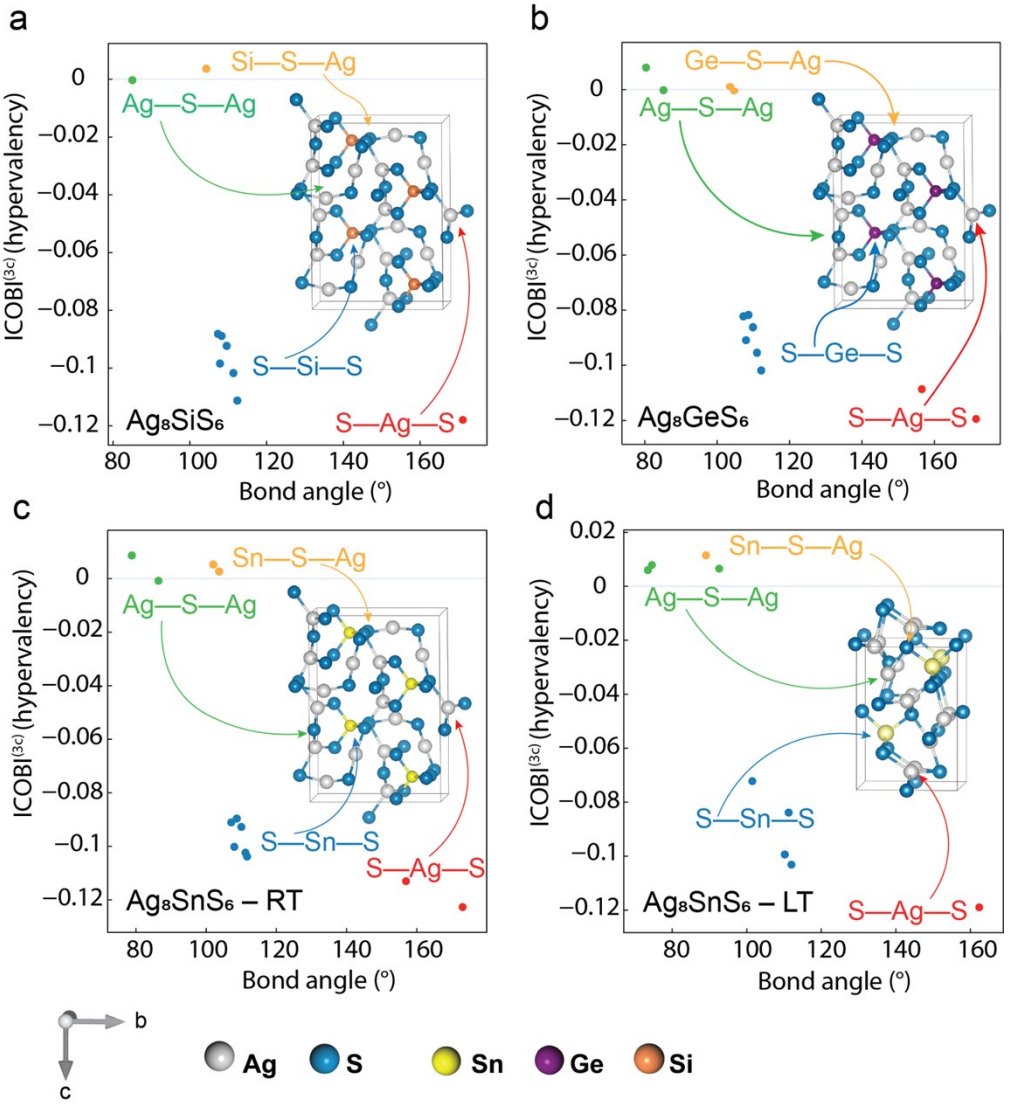

Figure S11. *Three-center ICOBI vs. bond angle plot of Ag_8TS_6 (T = Sn, Ge, Si).*

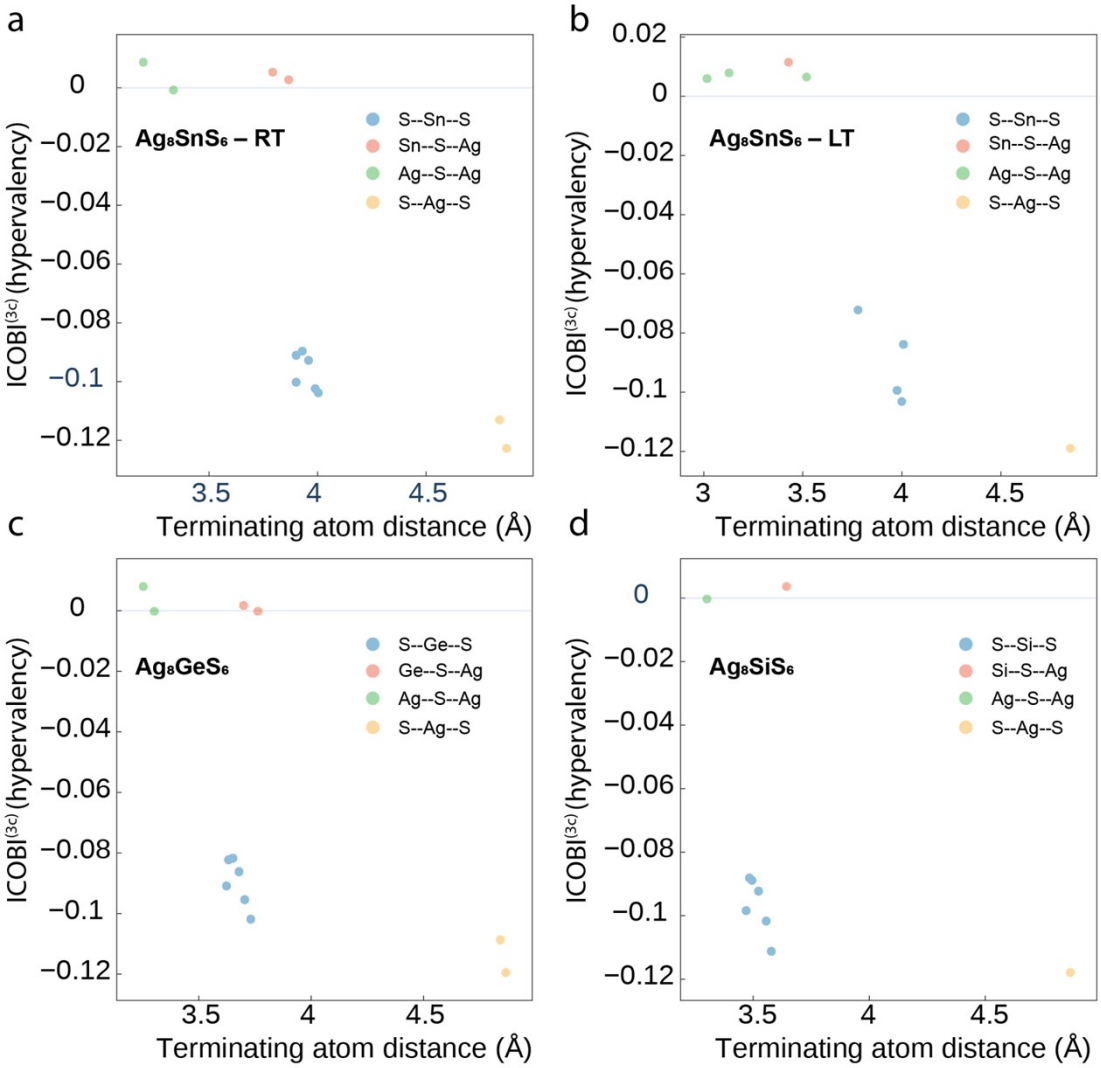

Figure S12. *Three-center ICOBI vs. terminating atom distance plot of Ag_8TS_6 (T = Sn, Ge, Si).*

As the three-center ICOBI$^{(3c)}$ corresponds to the hypervalency of the bonding electrons, negative values indicate electron-rich, and positive values correspond to electron-poor interactions.[6] It is noticeable that the interactions roughly split up into two categories: weak electron-poor and comparably strong electron-rich bonds. The electron-poor bonds are close to ICOBI$^{(3c)}$ = 0 and consist of Ag—S—Ag and Ag—S—*T* bonds, while the stronger electron-rich interactions exhibit ICOBIs$^{(3c)}$ between roughly −0.08 and −0.12. Here, it is striking that the S—*T*—S tetrahedral bonds show comparably strong bonds$^{(3c)}$, further contributing to their covalent character, even though the linear S—Ag—S bonds are favored. Hypervalency has been found and discussed in many polyanions and might therefore not be surprising here. However, it might be unexpected for a TS_4^{4-} polyanionic unit when assuming single bonds and a formal charge of –2 for S, as the octet rule would be perfectly fulfilled. We have to keep in mind that,

although quantitatively, the S—Ag—S and S—*T*—S bonds seem to have the same strength, in the context of their chemical environment, the bonds differ qualitatively. Compared to extended bonds like S—Ag—S, an ICOBI$^{(3c)}$ of around –0.1 in a local structure element like a tetrahedron can be seen as weak.[7] There is almost no significant difference in the three-center bonds of Ag_8SnS_6, Ag_8GeS_6, and Ag_8SiS_6, except that the Si-analogue shows fewer relevant S—Ag—S multi-center interactions than the other compounds, and therefore is a less dense bond network.

The bonding situation involving Ag and S resembles the one in the phase-change material [NaCl] GeTe.[8] In GeTe, it was found that the Te—Ge—Te bonds show an ICOBI$^{(3c)}$ value of around –0.1, while the Ge—Te—Ge ICOBI$^{(3c)}$ is exactly zero. The peculiar bonding situation in GeTe can be explained by constructively interfering orbital contributions for Te—Ge—Te and destructively interfering orbital contributions for Ge—Te—Ge (cf. Figure. 3 in [8]). A similar situation is found for the argyrodite compounds.

For example, in Ag_8SnS_6 (RT), the S—Ag—S bonds have dominating orbital contributions of S($3p_y$)—Ag(5s)—S($3p_x$) (−0.02026), S($3p_x$)—Ag(5s)—S($3p_y$) (−0.01288), S($3p_x$)—Ag(5s)—S(3s) (−0.01150), and S($3p_x$)—Ag(5s)—S($3p_x$) (−0.02862), while the Ag—S—Ag bond's leading orbital contributions Ag(5s)—S(3py)—Ag(5s) (+0.02194) and Ag(5s)—S($3p_x$)—Ag(5s) (−0.01536) are almost canceling each other out.

In Ag_8SnS_6 (LT), the Ag—S—Ag orbital contributions are all smaller than ±0.01, while the dominating S—Ag—S orbital contributions are S($3p_z$)—Ag(5s)—S(3s) (−0.01292), S($3p_z$)—Ag(5s)—S($3p_y$) (−0.03628) and S($3p_z$)—Ag(5s)—S($3p_z$) (−0.03566).

In Ag_8GeS_6, the S—Ag—S leading orbital contributions are S($3p_y$)—Ag(5s)—S($3p_x$) (−0.02136), S($3p_x$)—Ag(5s)—S($3p_y$) (−0.01276), S($3p_x$)—Ag(5s)—S(3s) (−0.01168), and S($3p_x$)—Ag(5s)—S($3p_x$) (−0.02612), while the Ag—S—Ag orbital contributions are Ag(5s)—S(3py)—Ag(5s) (+0.01798) and Ag(5s)—S($3p_x$)—Ag(5s) (−0.01298).

Finally, in Ag_8SiS_6, the S—Ag—S leading orbital contributions are S($3p_y$)—Ag(5s)—S($3p_x$) (−0.02174), S($3p_x$)—Ag(5s)—S($3p_y$) (−0.01346), S($3p_x$)—Ag(5s)—S(3s) (−0.01142), and S($3p_x$)—Ag(5s)—S($3p_x$) (−0.02488), while the Ag—S—Ag orbital contributions are Ag(5s)—S(3py)—Ag(5s) (+0.01598), Ag(5s)—S($3p_z$)—Ag(5s) (−0.00786) and Ag(5s)—S($3p_x$)—Ag(5s) (−0.00840).

Except for the expected difference in the distance of the terminating atoms of the tetrahedral bonds because of the different metal types, there is almost no difference in the three-center bonds of Ag_8SnS_6, Ag_8GeS_6, and Ag_8SiS_6.

Section S3: Thermal transport

The total thermal conductivity κ is calculated from the measured thermal diffusivity D following the equation $\kappa = D \cdot C_p \cdot \rho$, where ρ represents the geometrical density and C_p is the isobaric heat-capacity. The isobaric heat capacity was approximated using isochoric heat capacities derived from density-functional theory simulations. The total thermal conductivity comprises contributions from both the lattice thermal conductivity (κ_{lat}) and the electronic thermal conductivity(κ_e). The electronic thermal conductivity (κ_e) can be estimated using the Wiedemann-Franz law, $\kappa_e = L \cdot \sigma \cdot T$, where L is the Lorenz number, σ is the electrical conductivity, and T is the temperature.[9] For the Ag_8TS_6 (T = Si, Ge, Sn) argyrodites, the electrical conductivity (σ) is below the detection limit (minimum measurable value: 0.05 S/cm) of our four-probe measurement setup (SBA 458 instrument), making it unmeasurable. Therefore, the total thermal conductivity (κ) is assumed to be equivalent to the lattice thermal conductivity (κ_{lat}) for these systems. Thermal diffusivity (D) (**Figure S13**) and total thermal conductivity (κ) across the three compositions show similar results, with no significant variations observed.

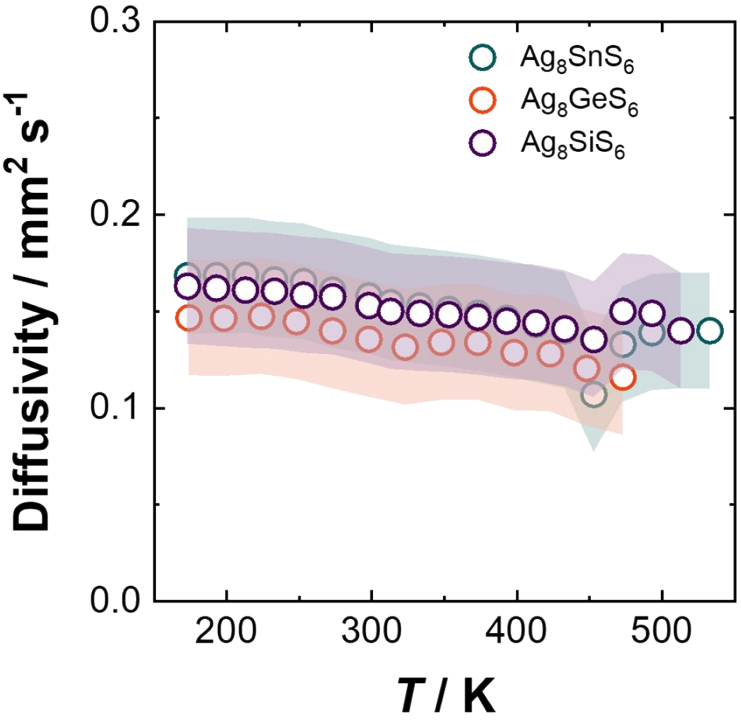

Figure S13. *Temperature-dependent thermal diffusivity (D) of Ag_8TS_6 (T = Si, Ge, Sn).*

Section S4: Synthesis and X-ray diffraction analysis of blocking electrode $RbAg_4I_5$

$RbAg_4I_5$ has previously been reported as an effective Ag^+ ion-conducting and electron-blocking electrode.[10] In this study, it is utilized to prevent electronic interference and enable accurate measurement of ionic conductivity of our Ag-based argyrodites. $RbAg_4I_5$ was synthesized via mechanochemical ball milling process. Stoichiometric amounts of RbI (Thermo Scientific, 99.8%) and AgI (Thermo Scientific, 99 %) were weighed inside an argon-filled glovebox under dark conditions and pre-mixed by hand grinding. The mixture was transferred into 80 mL zirconia ball milling cups, along with 5 mm diameter milling media (10:1 ball to reactant mixture mass ratio) and milled for 72 cycles at 400 rpm (10 minutes of milling followed by 10 minutes of rest per cycle). Upon completing the 72 cycles, the ball-milling cups were opened inside the glovebox, and the samples were taken and hand-ground in an agate mortar.

The X-ray diffraction pattern of powdered $RbAg_4I_5$ was measured and analyzed by Rietveld refinement using the TOPAS-Academic V7 software package[1], confirming a cubic structure with space group ($P4_132$) at 298 K (**Figure S14**). The observed phase fully accounts for the diffraction pattern and the refined lattice parameter, a = 11.2493(3) Å, agrees well with literature values,[11] verifying the successful synthesis and phase purity of the compound.

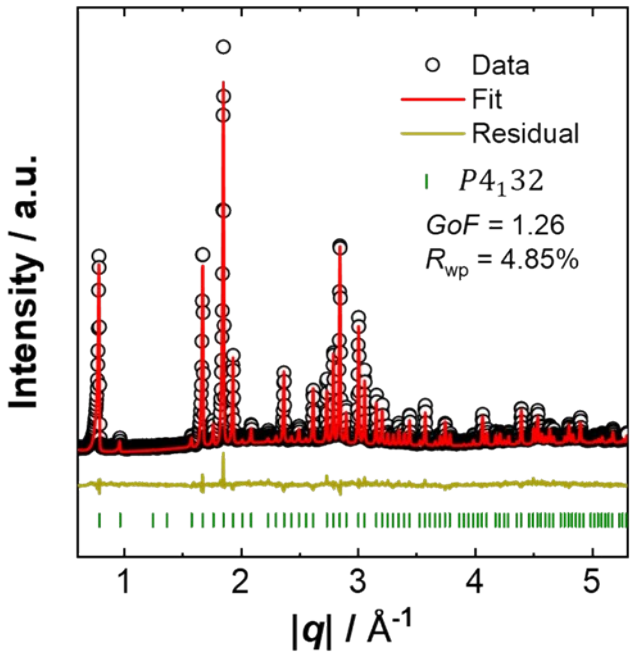

Figure S14. *X-ray diffraction patterns and corresponding Rietveld refinement results of $RbAg_4I_5$ at 298 K.*

Section S5: DC polarization and ion transport

Ag_8TS_6 (T = Si, Ge, Sn) argyrodites are known as mixed ionic-electronic conductors.[12] Therefore, to assess the electronic conductivity, electronic direct current polarization experiments were first carried out. The results indicate that the electronic conductivity of all three argyrodites lies in the range of 0.141×10^{-4} mS/cm to 0.0175 mS/cm, confirming minimal electronic contribution (**Figure S15)**. To ensure accurate determination of ionic conductivity, an electron-blocking, ion-conducting electrode ($RbAg_4I_5$)[3,13] was used to suppress electronic interference.

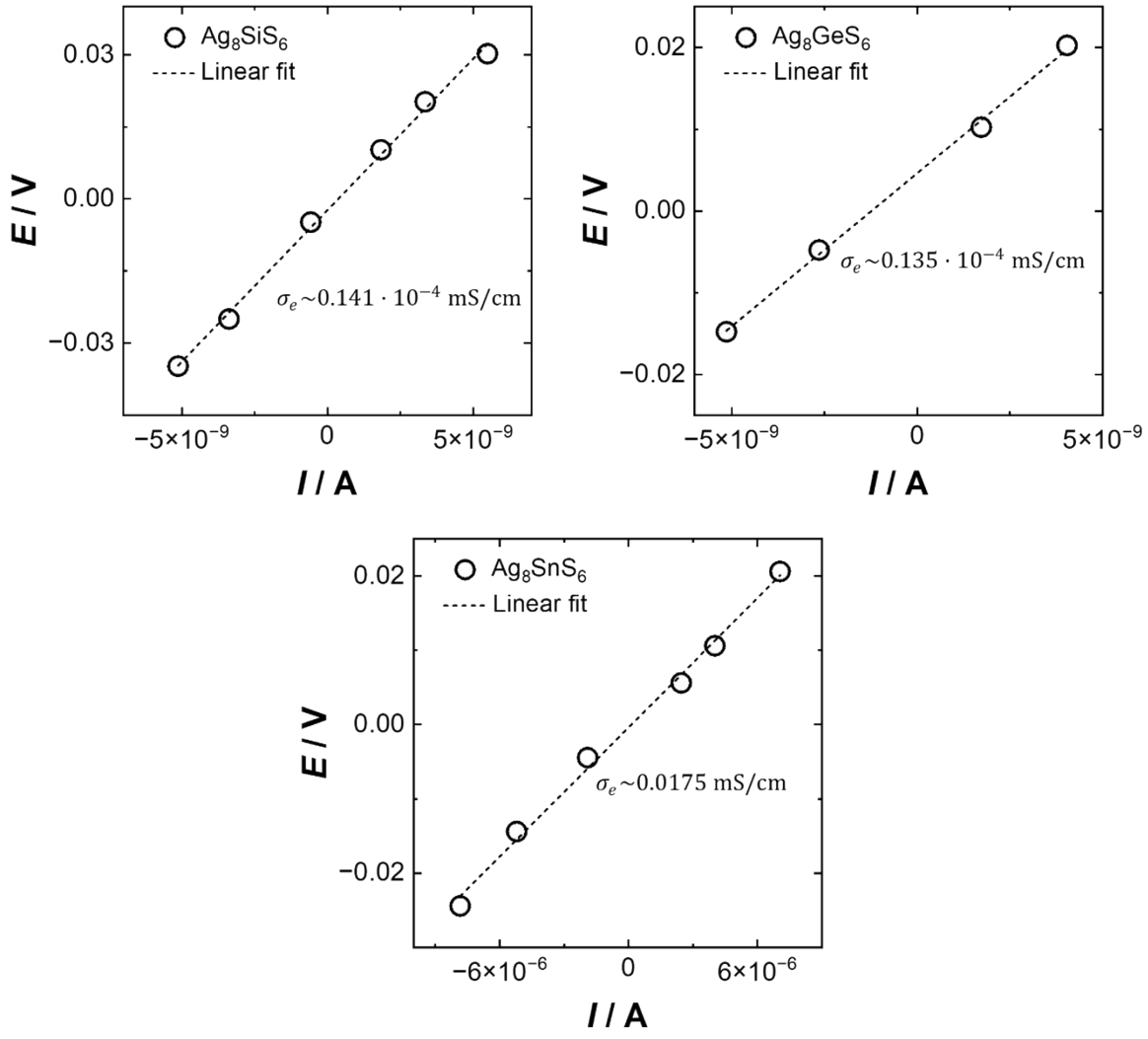

Figure S15. *The applied voltage versus current response of Ag_8TS_6 (T = Si, Ge, Sn), obtained from DC polarization measurements, is used to determine the electronic conductivity* (σ_e) *value.*

The impedance results of the electrode material $RbAg_4I_5$ and all Ag_8TS_6 (T = Si, Ge, Sn) argyrodites were analyzed using the RelaxIS 3 software package. The Nyquist plot of $RbAg_4I_5$ at 233 K is presented in **Figure S16a**. It was also employed in our previous work,[3] and is reanalyzed here for completeness. The impedance response of $RbAg_4I_5$ is characterized by an ohmic resistance (x-axis intercept), followed by a straight-line indicative of capacitive behaviour. The ionic conductivity of $RbAg_4I_5$ was found to be 173 ± 5 mS / cm, with an activation energy of 0.09 ± 0.02 eV, as illustrated by the Arrhenius plot (**Figure S16b**). The impedance responses of Ag_8TS_6 (T = Si, Ge, Sn) measured with blocking electrodes (thickness h = 0.08 cm) at 233 K are shown in **Figure S17a**. The spectra exhibit a semicircle at high frequencies and a tail at low frequencies. The high-frequency process is modelled using an equivalent circuit consisting of a resistor (R) in parallel with a CPE. To interpret the origin of the high-frequency resistance, the capacitance (C) of the process was evaluated. For a CPE with admittance Q and ideality factor α, the capacitance is given by:

$$C = \left(\frac{Q}{R^{\alpha - 1}}\right)^{1/\alpha} \tag{S1}$$

where R is the resistance parallel to the CPE. The extracted capacitance value for Ag_8TS_6 (T = Si, Ge, Sn) is approximately 10^{-11} F, indicating in-grain ionic conduction.[14] The low-frequency tail corresponds to the blocking effect of the electrodes. The high-frequency resistance primarily arises from the combined ionic transport through Ag_8TS_6 and the $RbAg_4I_5$ electrode layers. However, due to the thin electrode layer and high ionic conductivity of $RbAg_4I_5$, its contribution is negligible. Therefore, to accurately determine the intrinsic ionic conductivity of Ag_8TS_6, the resistance contribution of the electrode material is subtracted from the total resistance. The ionic conductivities of Ag_8TS_6 (T = Si, Ge, Sn) are evaluated across a range of temperatures and exhibited Arrhenius-type behavior (**Figure S18**). The obtained ionic conductivities are 0.081 ± 0.007, 0.065 ± 0.005, and 0.075 ± 0.008 mS/cm for Ag_8SnS_6, Ag_8GeS_6, and Ag_8SiS_6, respectively, at 298 K (errors represent standard deviations from triplicates). The activation energies for ion transport, calculated from Arrhenius plots (shown below in **Figure S18**), are nearly identical for all three argyrodites: 0.29 ± 0.02 eV. These results suggest that isovalent substitution at the T-site (Si, Ge, Sn) does not significantly affect ionic conductivity, a trend consistent with the behavior observed in the thermal transport properties. Literature study suggests that the relatively low obtained ionic conductivity in these

Ag^+ conducting argyrodites may be attributed to their crystal structures, where all Ag^+ positions are nearly fully occupied.[3,12] The variation of ionic and thermal conductivity with increasing temperature, measured within the same temperature range, is illustrated in **Figure S17b**. The room-temperature ionic conductivity values and the corresponding activation energies for ion transport are summarized in the table below (**Table S12**).

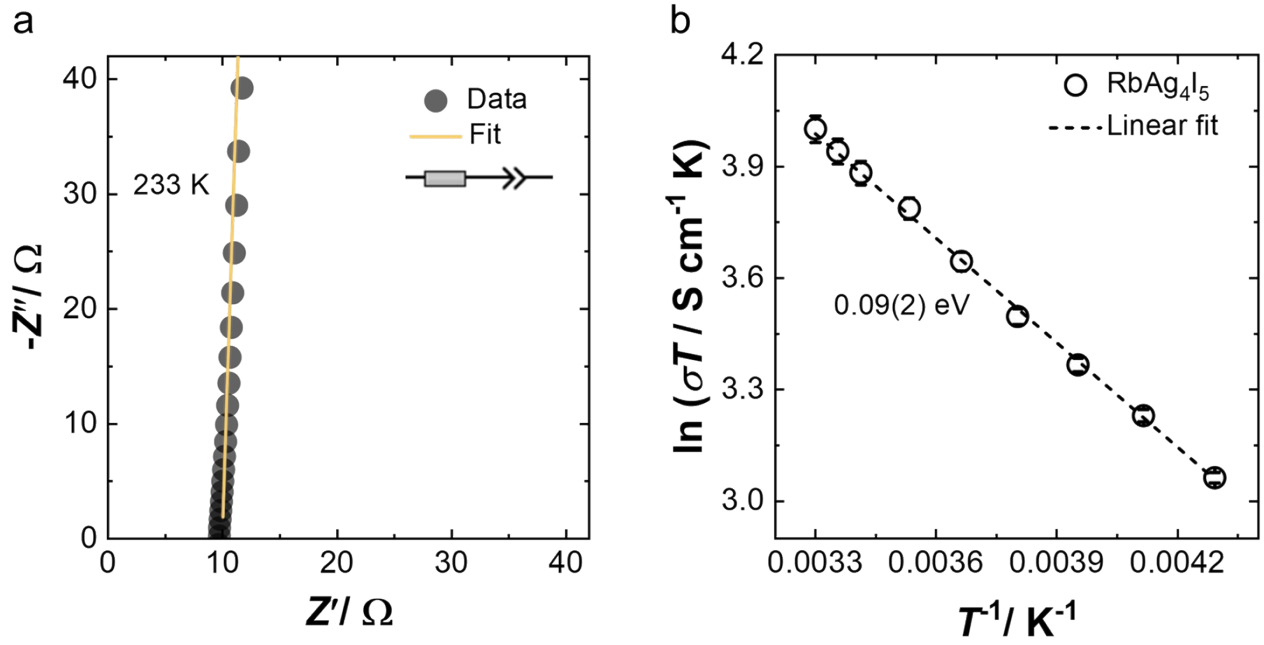

Figure S16. *a) Nyquist plots of $RbAg_4I_5$ at 233 K measured within the frequency range from 5 MHz to 1 Hz. The inset of the plot shows the equivalent circuit used to fit the data. b) Arrhenius plot of measured conductivities of $RbAg_4I_5$, indicating an activation energy of 0.09 eV for ion transport.*

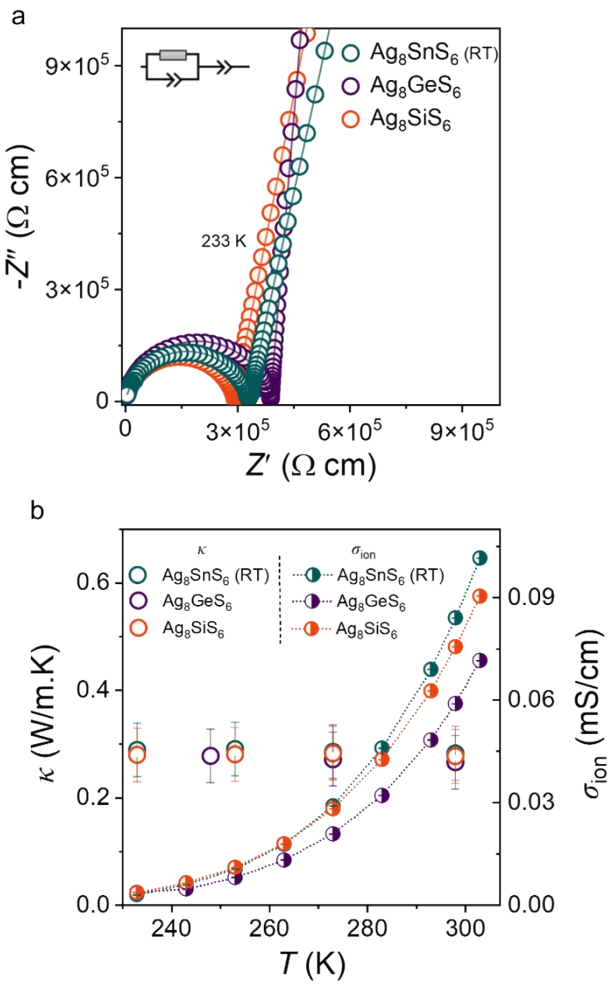

Figure S17*. a) Normalized Nyquist plots of Ag8TS6 (T = Si, Ge, Sn) recorded at 233 K, showing higher resistance values, which indicate lower ionic conductivity* (σ_{ion})*. b) The variation of thermal* (κ) *and ionic conductivity* (σ_{ion}) *with temperature, exhibiting no direct correlation between the two.*

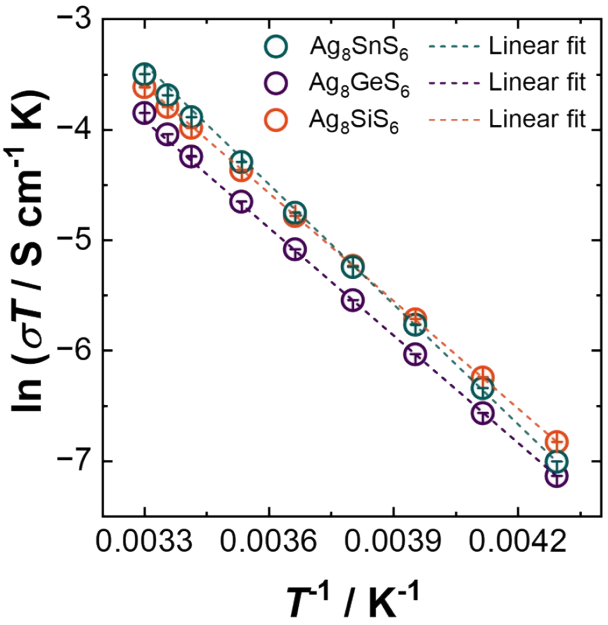

Figure S18. *Arrhenius plots of measured conductivities of Ag_8TS_6 (T = Si, Ge, Sn), indicating an activation energy of 0.29 ± 0.2 eV for ion transport.*

Table S12. *The ionic conductivities at 298 K and the obtained activation energy barriers for ion transport in Ag_8TS_6 (T = Si, Ge, Sn).*

***T* in Ag_8TS_6**	**σ_{ion} at 298 K / mS/cm**	**E_a / eV**
Si	0.075 ± 0.008	0.27 ± 0.02
Ge	0.065 ± 0.005	0.28 ± 0.01
Sn	0.081 ± 0.007	0.31 ± 0.02

Section S6: Thermal transport - Computations

Sound and group velocities – Discussion of the results

Sound velocities and Debye temperatures for Ag_8SnS_6, Ag_8GeS_6, and Ag_8SiS_6 were calculated through elastic properties simulations (bulk and shear modulus). The details of the calculations are discussed in the next section. In general, related argyrodites with low lattice thermal conductivity, e.g., selenides and tellurides, exhibit mean sound velocities between 1000 and 1500 m/s.[15] The computed mean sound velocities (**Table S14**) show a slight decrease with increasing atomic mass, having a good agreement with the measured mean sound velocities (

v_m^*). As the bonding analysis in the main text already suggested, we find no significant differences in the speed of sound for the three different compounds. Therefore, the thermal conductivities derived from models based solely on sound velocities and material densities will be almost identical (**Table S15).**

To complement the sound velocity analysis, we also obtained group velocities from harmonic phonon calculations. Again, no significant difference between the argyrodite compounds was observed. Here, the phonon group velocities (**Figure S19**) show higher velocities for low-frequency modes, which are mainly dominated by Ag^+ ions vibrations due to their low bonding interaction. Therefore, no substantial distinctions between the compounds from the sound velocities and group velocities can be concluded.

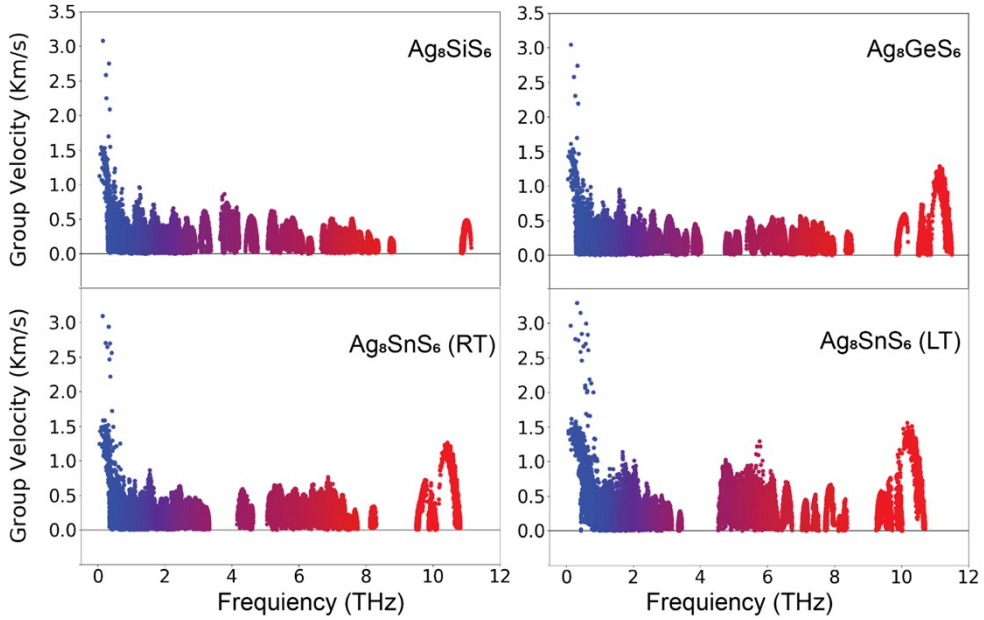

Figure S19. *Phonon group velocity for Ag_8TS_6 (T= Si, Ge, and Sn). Notably, higher group velocities are observed at the low-frequency region, which are again mainly dominated by the Ag^+ vibration and may influence the low lattice thermal conductivity behaviour. The colors indicate band indices with ascending order of phonon frequencies*

The Debye temperature and frequency, estimated from both theoretical and experimental results, yield low values as an indication of low lattice thermal conductivity, which is in line with Slack's theory.[16–18] The calculated Debye temperatures and frequencies **(Table S13)** for Ag_8TS_6 (*T*= Si, Ge, and Sn) also show a gradual decrease with increasing atomic mass. Nevertheless, the variations in both experimental and theoretical values are minor and do not

indicate any significant differences between the three different compounds. Even room-temperature and low-temperature Ag_8SnS_6 show a very similar tendency.

Sound velocity – Computational Details

Debye temperature (θ) and frequency (ω_D) can be estimated either from elastic properties calculations or derived from phonon computations as described in the main text. In this work, we used the phonon-based reduced Debye frequency, which corresponds to the acoustic Debye frequency $(\omega_{AC} = N^{-1/3}\omega_D)$, where *N* is the number of atoms in the unit cell. This frequency limit is more suitable for capturing the anharmonicity of acoustic phonons, which are the main contributors to phonon-phonon scattering and thermal transport properties.

Table S13. *Debye temperatures obtained through elastic property calculations* (Θ_{EL}) *and phonon computations, including all phonon modes* $(\Theta_{phonon,})$ *and acoustic modes* (Θ_{AC}) *compared with Debye temperature derived from experimental measurements* Θ_{Exp}*. We note here that* Θ_{phonon} *of* Ag_8SiS_6 *is unexpectedly high which might be related to the harmonic approximation or the level of theory used here.*

***T* in Ag_8TS_6**	Θ_{EL} **(K)**	Θ_{phonon} **(K)**	Θ_{AC} **(K)**	Θ_{Exp} **(K)**
Si	170	227	94	163.8±5.5
Ge	167	173	82	176.0±7.1
Sn (RT)	160	162	78	163.0±6.3
Sn (LT)	172	158	98	--

For all Ag_8TS_6 (*T*= Si, Ge, and Sn) compounds, we compare sound velocities calculated from two computational approaches (derived from elastic and phonon calculations) with our experimental measurements. For Ag_8GeS_6 and Ag_8SnS_6 (RT), both computational and experimental results show no significant differences. In contrast, Ag_8SiS_6 exhibits more pronounced discrepancies between our calculations and experimental data. This is especially true for the results derived from phonon calculations.

Table S14. *Sound velocity* (v_l, *and* v_t) *derived from elastic tensor calculations.* v_m *were obtained following Eq S2.* v_{phonon} *is the sound velocity calculated from phonon calculation and using Eq. 2 from the main text. Here,* v_m^* *is the experimental mean sound velocity at 300 K (this study). Further details on the elastic tensor calculation are provided below.*

T **in** Ag_8TS_6	v_l **(m/s)**	v_t **(m/s)**	v_m **(m/s)**	v_{phonon} **(m/s)**	v_m^* **(m/s)**
Si	2982.68	1389.15	1564.27	2087	1487±50
Ge	2960.67	1368.95	1542.06	1601	1602±65
Sn (RT)	2923.28	1332.50	1501.98	1513	1501±58
Sn (LT)	3042.83	1417.60	1596.28	1476	--

$$v_m = \left[\frac{1}{3}\left(\frac{2}{v_t^3} + \frac{1}{v_l^3}\right)\right]^{-1/3} \quad \text{(S2)}$$

The elastic properties were calculated with the workflow implemented in atomate2.[19,20] After an initial structural optimization, the structure is strained along the six independent strain directions (*xx*, *yy*, *zz*, *yz*, *xz*, and *xy*). Here, multiple strain magnitudes are applied, and additionally, symmetry is used to reduce the number of calculations. The components of the Green-Lagrange strain tensor are denoted by E_{ij}. Then, for each of these strained structures, the stress tensor is calculated. We represent the components of the stress tensor by S_{ij}. The stresses and strains are then used to fit an elastic tensor, which is a fourth-rank elastic tensor. The relationship between stresses and strains via the elastic tensor is given in the following equation:

$$\begin{bmatrix} S_{11} \\ S_{22} \\ S_{33} \\ S_{23} \\ S_{13} \\ S_{12} \end{bmatrix} = \begin{bmatrix} C_{11} & C_{12} & C_{13} & C_{14} & C_{15} & C_{16} \\ C_{12} & C_{22} & C_{23} & C_{24} & C_{25} & C_{26} \\ C_{13} & C_{23} & C_{33} & C_{34} & C_{35} & C_{36} \\ C_{14} & C_{24} & C_{34} & C_{44} & C_{45} & C_{46} \\ C_{15} & C_{25} & C_{35} & C_{45} & C_{55} & C_{56} \\ C_{16} & C_{26} & C_{36} & C_{46} & C_{56} & C_{66} \end{bmatrix} \begin{bmatrix} E_{11} \\ E_{22} \\ E_{33} \\ 2E_{23} \\ 2E_{13} \\ 2E_{12} \end{bmatrix} \quad \text{(S3)}$$

One row of the elastic tensor is then calculated via a linear fit of the calculated stresses against the range of applied strains. From the elastic tensor, bulk and shear modulus can be obtained.

The bulk modulus for the polycrystalline material $K_{VRH}$was obtained as the average of the upper (K_V) and lower (K_R) bounds of it for polycrystalline materials that can be computed with the following equations:

$$s_{ij} = C_{ij}^{-1} \quad \text{(S4)}$$

$$9K_V = (C_{11} + C_{22} + C_{33}) + 2(C_{12} + C_{23} + C_{31}) \quad \text{(S5)}$$

$$1/K_R = (s_{11} + s_{22} + s_{33}) + 2(s_{12} + s_{23} + s_{31}) \quad \text{(S6)}$$

$$2K_{VRH} = (K_V + K_R) \quad \text{(S7)}$$

Similarly, the shear modulus for the polycrystalline material (G_{VRH}) was obtained as the average of the upper (G_V) and lower (G_R) bound of it for polycrystalline materials that can be computed with the following equations:

$$15G_V = (C_{11} + C_{22} + C_{33}) - (C_{12} + C_{23} + C_{31}) + 3(C_{44} + C_{55} + C_{66}) \quad \text{(S8)}$$

$$\frac{15}{G_R} = 4(s_{11} + s_{22} + s_{33}) - 4(s_{12} + s_{23} + s_{31}) + 3(s_{44} + s_{55} + s_{66}) \quad \text{(S9)}$$

$$2G_{VRH} = (G_V + G_R) \quad \text{(S10)}$$

Based on these bulk and shear moduli of the polycrystalline materials, the sound velocities are computed as described and implemented as a part of ref [21]:

$$v_L = \left(\frac{K + 4/3G}{\rho}\right)^{1/2} \quad \text{(S11)}$$

$$v_T = \left(\frac{G}{\rho}\right)^{1/2} \quad \text{(S12)}$$

The corresponding implementations can be found in pymatgen[22].

Table S25. *Calculated elastic tensor components in GPa.*

***T* in Ag_8TS_6**	C_{11}	C_{12}	C_{13}	C_{22}	C_{23}	C_{33}	C_{44}	C_{55}	C_{66}
Si	44.34	30.51	29.72	65.63	30.89	46.60	8.64	14.93	13.23
Ge	45.11	32.86	29.96	64.68	31.29	46.49	8.22	15.07	14.68

Sn (RT)	47.64	34.71	30.59	59.86	29.48	43.49	7.47	15.07	15.25
Sn (LT)	71.08	40.57	34.94	43.04	28.36	52.34	12.97	12.63	17.04

The elastic constants reported in **Table S15** are relatively small, which explains the low sound velocities discussed above. Moreover, low elastic constants indicate that the lattice offers weak resistance to both tensile and shear deformations, reflecting a mechanically soft bonding framework. This mechanical softness is consistent with the reduced sound velocities and weak bonding in all Ag_8TS_6 (T= Si, Ge, and Sn) compounds.

Lattice thermal conductivity in compounds with high anharmonicity

The diversity in composition and structure, as well as the complexity of the materials involved, makes it difficult to determine the lattice thermal conductivity using a single computational model. Thermal conductivity models range from simple empirical relationships to complex quantum mechanical calculations. For instance, it is possible to estimate the minimum thermal conductivity using the Cahill[23] and Agne[24] models. Cahill follows Einstein's notion of lattice vibration. The model assumes that the individual oscillators vibrate independently, and that the phonon relaxation time is half the vibration period. Given the inverse correlation between minimum thermal conductivity and speed of sound, a lower minimum thermal conductivity is therefore expected when the speed of sound is low. On the other hand, Agne proposed a diffusion-mediated model in which the phonon density of states is used and it is assumed that all vibrations behave as diffusons with a jump distance equal to a characteristic interatomic distance. Both models can be computed as follows:

$$\kappa_{min}^{Cahill} = \frac{1}{2.48} k_B \left(\frac{N\rho N_A}{M}\right)^{2/3} (v_L + 2v_T) \quad \text{(S13)} \qquad \kappa_{min}^{Agne} = 0.76 n^{2/3} k_B \frac{1}{3} (v_L + 2v_T) \quad \text{(S14)}$$

Where k_B and N_A are the Boltzmann and Avogadro constants, N is the number of atoms, ρ is the density, and v_L and v_T are the longitudinal and transversal sound velocities, respectively.

The Slack model, [16,17,25] as mentioned in the main text, is also an alternative to compute the lattice thermal conductivity of materials. Here, the acoustic modes play an important role in the thermal transport process and the lattice thermal conductivity can be computed as:

$$\kappa_{Slack} = A\frac{\bar{M}\delta n^{1/3}\Theta_{AC}^{\ 3}}{\gamma^2 T} \tag{S15}$$

Where $\bar{M}$ is the average atomic mass, δ is the average volume per atom, n is the number of atoms in the unit cell, Θ_{AC} is the acoustic Debye temperature, T is the absolute temperature, k_B and $\hbar$ are the Boltzmann and Planck constants, respectively, and A is the Slack coefficient, which is dependent on the anharmonicity of the structure, represented by the Grüneisen parameter.

$$A = \frac{2.436 \times 10^{-8}}{1 - \frac{0.514}{\gamma} + \frac{0.228}{\gamma^2}} \tag{S16}$$

This model can provide helpful information about lattice thermal conductivity; however, it tends to be generally overestimated compared to experimental data. This discrepancy can be related to the A coefficient, but can be effectively corrected by scaling by a factor, as proposed by Qin[26]:

$$A = \frac{0.609 \times 10^{-6}}{1 - \frac{0.514}{\gamma} + \frac{0.228}{\gamma^2}} \tag{S17}$$

In the two-channel model by Simoncellli et al.[27], the heat flux and thermal conductivity are expressed by a matrix, where the diagonal part describes the phonon modes conducting heat as propagating waves known as the phonon-gas channel, and the non-diagonal part represents the phonons conducting energy diffusely, known as the diffuson-channel or "random walk". The sum of those two channels gives the total lattice thermal conductivity.

$$\kappa = \kappa_{ph} + \kappa_{Diff} \tag{S18}$$

Studies of similar argyrodite-type materials suggest that the Ag^+ vibration has a non-propagating diffuson-like character.[10] To corroborate this, we also compute the thermal conductivity following the recent two-channel model developed by Xia et al [28], which uses the harmonic phonons and considers that each phonon's lifetime is half of its vibration period:

$$\kappa_{Xia}^{min} = \frac{\pi\hbar^2}{\kappa_B T^2 V N_q} \sum_q \sum_{s,s'} \frac{\left(\omega_q^s + \omega_q^{s'}\right)^2}{2} v_q^{s,s'} \otimes v_q^{s',s} \frac{\omega_q^s n_q^s \left(n_q^s + 1\right) + \omega_q^{s'} n_q^{s'} \left(n_q^{s'} + 1\right)}{4\pi^2 \left(\omega_q^{s'} - \omega_q^s\right)^2 + \left(\omega_q^s + \omega_q^{s'}\right)^2} \quad \text{(S19)}$$

In **Table S16,** we show the lattice thermal conductivity following all models mentioned above. Cahill, Agne and Xia models accurately estimate the minimum lattice thermal conductivity (κ_{min}) for all the argyrodite compounds. These models are valuable, but their applicability is inherently limited to estimating theoretical lower bounds. In addition, the scaled Slack model reduced the overestimation shown in the original Slack model and also agrees with the lower thermal conductivity, especially at 600K.

Table S16. *Comparison of lattice thermal conductivity following different models.*

	Thermal conductivity (W/mK)							
			κ_{Xia}^{min} **(T=600K)**					
***T* in Ag_8TS_6**	κ_{Cahill}^{min}	κ_{Agne}^{min}	κ_{diff}	$\kappa_{phonons}$	κ_{Total}^{min}	κ_{Slack}	$\kappa_{Scaled-Slack}$	κ_{exp}^{min} *
Si	0.428	0.269	0.260	0.010	0.271	3.26	0.82	0.411±0.024
Ge	0.420	0.264	0.235	0.011	0.245	0.73	0.18	0.434±0.030
Sn (RT)	0.402	0.253	0.222	0.011	0.233	0.91	0.23	0.391±0.025
Sn (LT)	0.421	0.265	0.202	0.020	0.221	2.41	0.60	

*κ_{exp}^{min} minimal lattice thermal conductivity was derived from sound velocity measurements at 300K

In contrast to some of the above approximations, our full ab initio model explicitly incorporates anharmonic effects, enabling the prediction of temperature-dependent lattice thermal conductivity. Before estimating the thermal conductivity with the Grüneisen parameter-based approach, we compare the phonon lifetimes obtained from the analytical model, foundation machine-learned interatomic potentials (MACE-MP-03b), and the Grüneisen parameter-based approach. In **Figure S20a**, at 10K, the analytical model shows that both point-defect and boundary scattering have a strong impact on the phonon lifetimes, and consequently, influence the material's thermal conductivity and phonon transport properties. This observation is consistent with the trend of the phonon channel shown in **Figure 5d** in the main text. Here, MACE-MP-03b and Grüneisen models also exhibit reasonable agreement with the analytical model when point-defect and boundary scattering are subtracted. At 300K (**Figure S20b**), the effect of the point-defect and boundary scattering is less evident from the analytical model, but some differences are still present in both computational approaches. We anticipate that these differences in the lifetimes will also be present in the predicted lattice thermal conductivity,

especially at lower temperatures. Nevertheless, at 300K, the agreement between the models improves, which is also reflected in the close values of the calculated lattice thermal conductivity. A complete comparison of the lattice thermal conductivity of Ag_8GeS_6 is also presented in **Figure S22** and **Table S17**.

Additionally, we investigated the impact of different cutoff frequencies for the average Grüneisen parameter. As shown in **Figure S20b**, focusing on the acoustic modes yields good agreement with the experimental Grüneisen parameter, particularly for the Ag_8GeS_6 and Ag_8SnS_6 argyrodites. For Ag_8SiS_6, a slight deviation is observed, consistent with the differences shown in the Grüneisen parameter plot in **Figure 4** in the manuscript. We employed the average derived from the acoustic Grüneisen parameter in the subsequent calculations of lattice thermal conductivity.

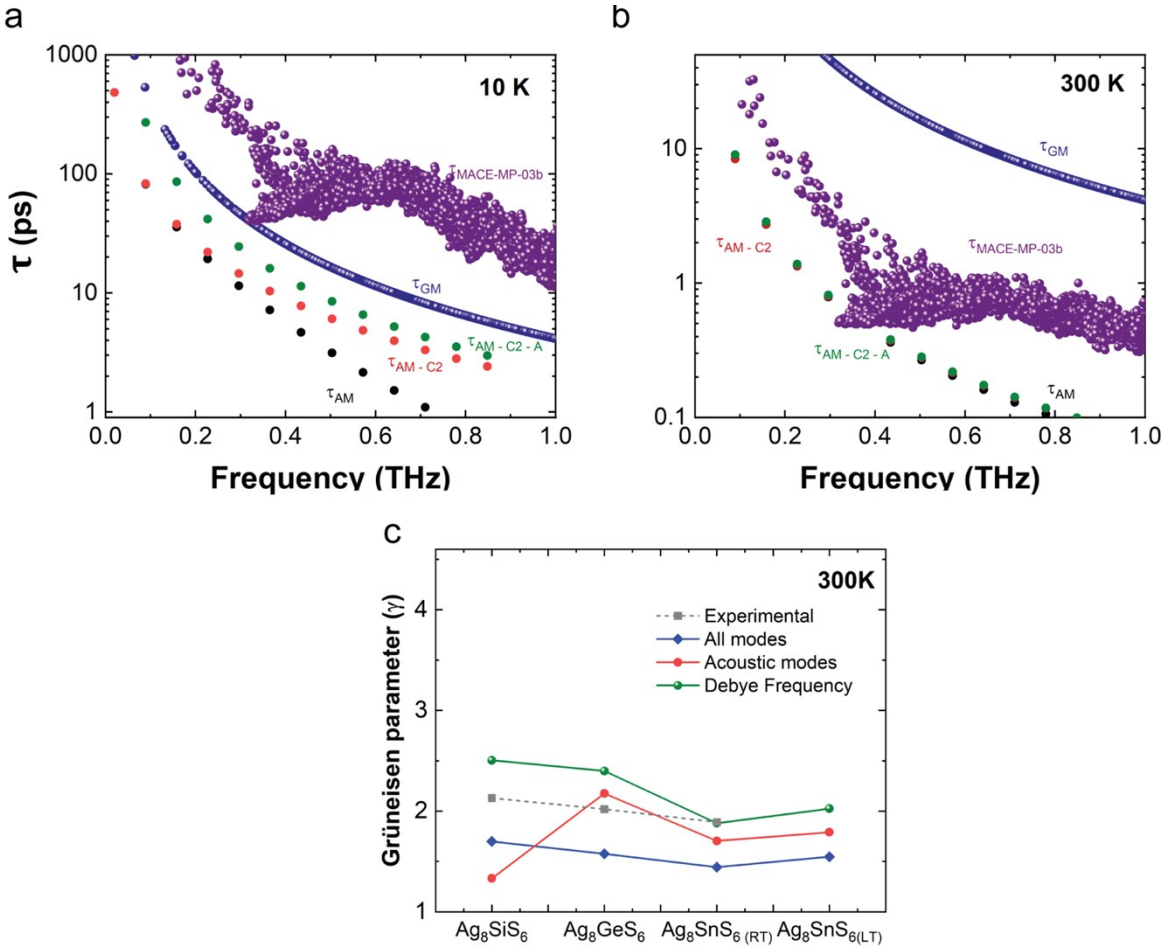

***Figure S20**. a) Phonon lifetimes as a function of the phonon vibrational frequencies for Ag_8GeS_6 at 10K. Here, point defects and boundary scattering have a considerable influence on the phonon lifetimes in the analytical model. The foundation model MACE-MP-03b and*

Grüneisen model present reasonable agreement with it. b) Phonon lifetimes at 300K for the same models mentioned before. The two computational models agreed well with the phonon lifetimes predicted by the analytical model. c) Average Grüneisen parameter for Ag_8TS_6 (T = Si, Ge, Sn), evaluated with different frequency cutoffs. Here, a q-mesh of 10×20×14 was found to be optimal and subsequently used for the lattice thermal conductivity calculations.

Finally, using the Grüneisen model to compute the lattice thermal conductivities shows very good agreement with the experimental results for the sulfide-argyrodite compounds, as illustrated in **Figure S21** and **Figure 5a.** Our computational results show a slight deviation for Ag_8SiS_6 from experiment. These deviations are attributed to variations in the mode-dependent Grüneisen parameters.

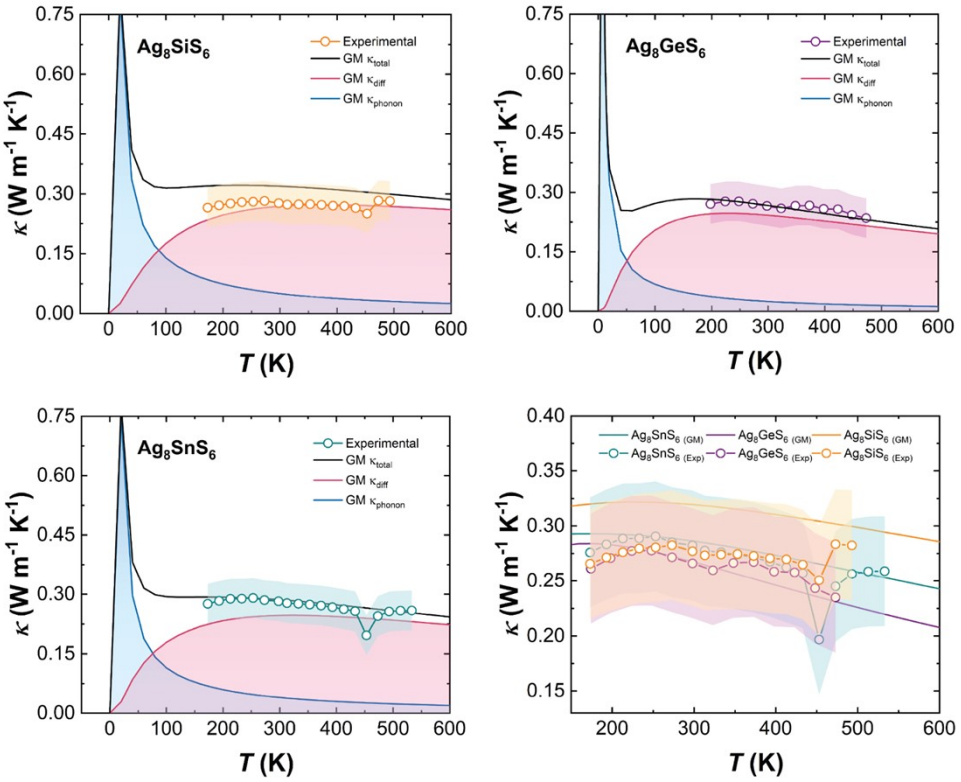

Figure S21. *Two-channel model using our proposed Grüneisen model for the Ag_8TS_6 (T = Si, Ge, Sn) compared with our experimental measurements.*

For the Ag_8GeS_6 argyrodite, a full comparison of the total lattice thermal conductivity is presented in **Figure S22** and **Table S17-S18.** The two models developed in this work (Grüneisen and ML) show minor differences, and they remain consistent with the experimental results, with particularly strong agreement observed at temperatures above 200 K. Additionally,

in **Table S19,** we include the fitting parameters from the analytical model presented in **Figure 5a** in the main text.

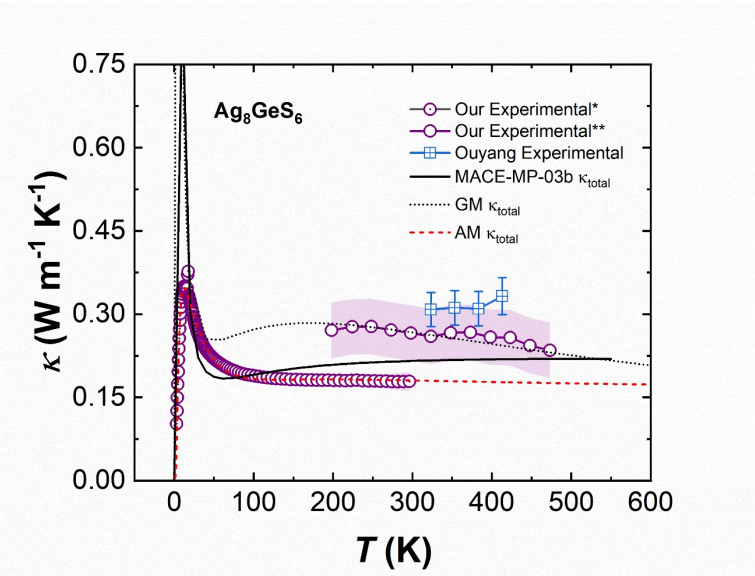

Figure S22. *Total lattice thermal conductivity comparison for Ag_8GeS_6: Analytical, Grüneisen, and foundation MACE-MP-30b model versus experimental data (this work and literature).*

Table S17. *Comparison of lattice thermal conductivity of Ag_8GeS_6 argyrodite obtained from the Grüneisen model, analytical model fitted to low-temperature experimental data from our work, and other experimental measurements (Ouyang and this work).*

Ag_8GeS_6	$\kappa_{(300K)}$ (W m^{-1} K^{-1})
Mace-MP-03b	0.216
Full Analytical model	0.181
Grüneisen model	0.267
Our Exp**	0.266 ± 0.050
Ouyang $_{exp}$	0.274 ± 0.028
Ouyang $_{comp}$	0.312

Table S18. *Comparison of the Xia, our Grüneisen model, and experimental results for Ag_8GeS_6. The phonon channel is more pronounced in our Grüneisen-based model.*

	Lattice thermal conductivity (W/mK)						
	κ_{Xia}^{min} (T=400K)			κ_{GM}* (T=400K)			$\kappa_{Exp\ (T=433K)}$
***T* in Ag_8TS_6**	κ_{diff}	κ_{ph}	κ_{Total}^{min}	κ_{diff}	κ_{ph}	κ_{Total}^{min}	
Si	0.257	0.010	0.267	0.273	0.038	0.310	0.267 ± 0.05
Ge	0.232	0.010	0.243	0.227	0.019	0.246	0.252 ± 0.05
Sn (RT)	0.220	0.011	0.231	0.244	0.030	0.273	0.257 ± 0.05
Sn (LT)	0.199	0.020	0.219	0.219	0.043	0.262	-

* GM corresponds to the Grüneisen-based model

Table S19. *Fitting parameter extracted from the analytical model of the Ag_8GeS_6 argyrodite. C_1 represents phonon-phonon scattering, C_2 is the point-defect scattering coefficient, A is related to boundary scattering, and P is related to the overlap integral between the linewidths of two proximal phonon modes.*

Fitting parameters	
C_1	$11.801 \pm 0.284 \times 10^{-16}$ s K^{-1}
C_2	$15.431 \pm 1.848 \times 10^{-40}$ s^3
P	0.387 ± 0.007
A	0.015 ± 0.002

Validation of the Grüneisen model

To validate our Grüneisen-based model, we computed the lattice thermal conductivity for similar argyrodite materials. Here, Ag_8GeSe_6 and Ag_9GaSe_6 were considered. First, we started with the phonon dispersion curves and Grüneisen parameter plots for both compounds (**Figure S23Fehler! Verweisquelle konnte nicht gefunden werden.**).

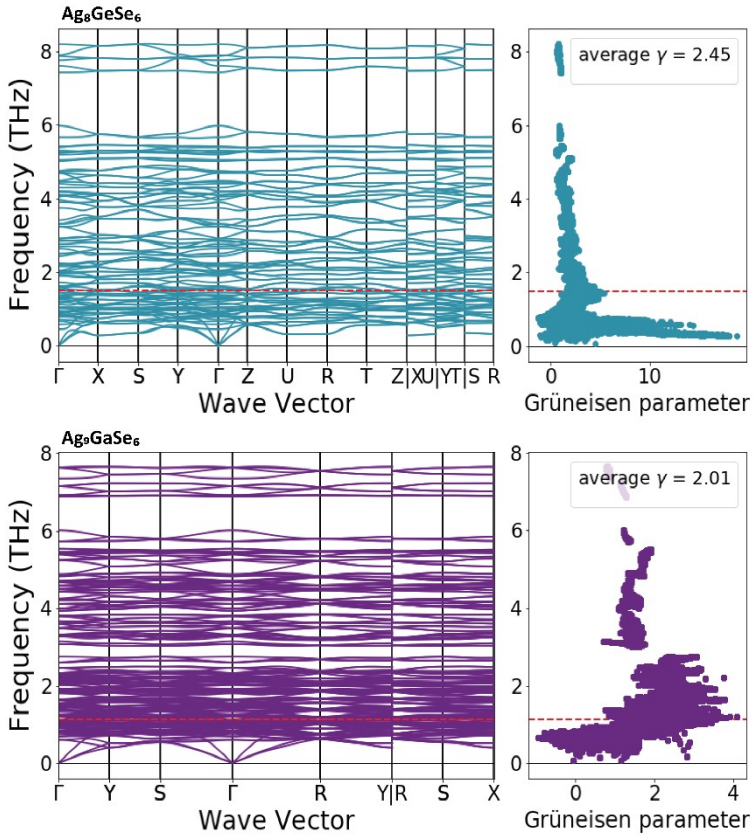

Figure S23. *Phonon band structure and Grüneisen parameter for Ag_8GeSe_6 and Ag_9GaSe_6*

The lattice thermal conductivity calculated with our model, which includes only the phonon-phonon scattering, reproduces the experimental result with good enough accuracy, considering the associated experimental uncertainties for both compounds. In **Figure S24 a and b**, we show the two-channel model for Ag_8GeSe_6. At low temperatures, we observe an overestimation in the phonon channel, which affects the total lattice thermal conductivity. However, this is not surprising as we neglect point-defect and microstructure effects in our Grüneisen-based model. In the room- and high-temperature (between 250-600K) range, the thermal conductivities show better agreement with the analytical model and the experimental values reported by Bergnes.[29] Similar results were observed for the Ag_9GaSe_6. Overall, the total lattice thermal conductivity for both structures are within the expected error margins, supporting the reliability and accuracy of the results.

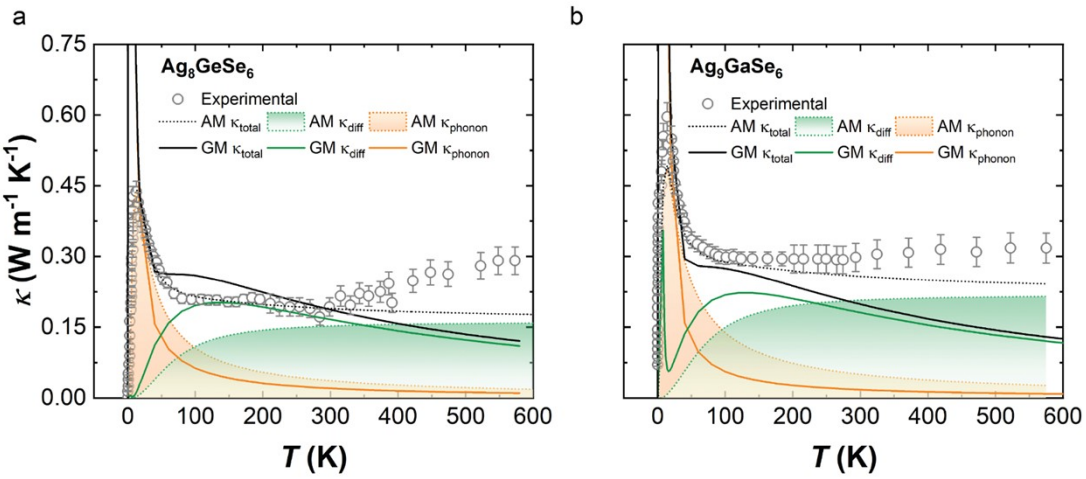

***Figure S24**. Comparison of our proposed Grüneisen-based two-channel model compared with the experimental and analytical model published by Bergnes[29] for both a) Ag_8GeSe_6 and b) Ag_9GaSe_6 argyrodites.*

Section S7: Possible phase transition

When performing the quasi-harmonic approximation, one of the expanded volume structures of $Ag_8Sn_1S_6$ shows a new possible phase transition, which, to our knowledge, has not been demonstrated experimentally. The phonon dispersion curve and PDOS, show the softening of the modes at expanded volume (typically connected to a higher temperature), leading to a possible new phase transition or dynamic stability. The new phase has the same space group as the RT structure ($Pna2_1$) and we can represent it with the same unit cell. The primitive unit cell that we chose for representation contains 60 atoms, which caused 180 phonon modes. A small expansion in the cell is observed due to the change in the position and coordination environments of the Ag atoms (**Figure S25**). In **Table S20**, we report the different coordination environments. Ag1 and Ag2 change to linear coordination from trigonal planar and tetrahedral, respectively. Another change is observed in Ag6 and Ag8, where the triangular non-coplanar environments change to trigonal planar and tetrahedral coordination environments. The coordination environments were again determined by quantum-chemical bonding analysis with LOBSTER and LobsterPy.

***Table S20.** Atomic positions and inequivalent site fractional coordinates of the possible phase transition of Ag_8SnS_6.*

Atom	POSCAR Position	Wyckoff Positions	x	y	z	Coordination Environment
Ag1	Ag1	4a	0.041	0.016	0.062	Linear
Ag2	Ag5	4a	0.026	0.142	0.324	Linear

Ag3	Ag9	4a	0.132	0.261	0.780	Trigonal Planar
Ag4	Ag13	4a	0.230	0.990	0.006	Trigonal Planar
Ag5	Ag17	4a	0.267	0.108	0.337	Linear
Ag6	Ag21	4a	0.266	0.353	0.107	Trigonal Planar
Ag7	Ag25	4a	0.405	0.914	0.584	Linear
Ag8	Ag29	4a	0.444	0.044	0.435	Tetrahedral
Sn1	Sn33	4a	0.130	0.712	0.761	Tetrahedral
S1	S37	4a	0.999	0.269	0.637	Tetrahedral
S2	S41	4a	0.129	0.256	0.004	Trigonal bipyramidal
S3	S45	4a	0.121	0.454	0.385	See-saw like
S4	S49	4a	0.248	0.207	0.629	Tetrahedral
S5	S53	4a	0.385	0.269	0.259	Square pyramidal
S6	S57	4a	0.361	0.457	0.899	Triangular non-coplanar

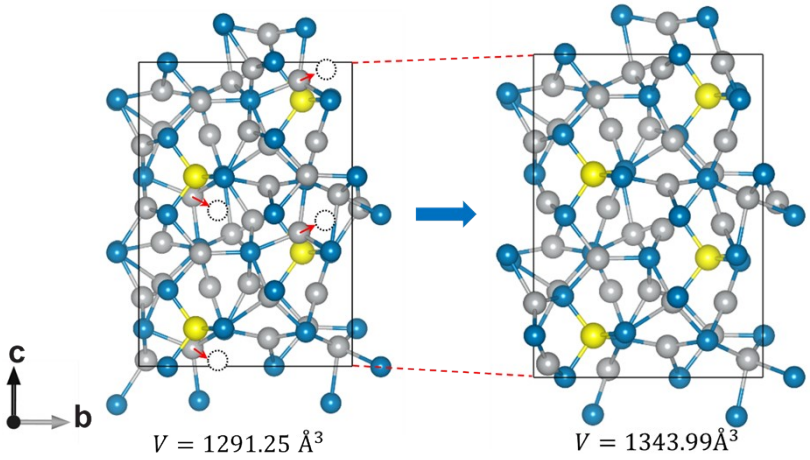

***Figure S25**. Structure change of the possible phase transition. A volume expansion is observed in Ag_8SnS_6 argyrodites.*

The shape of the phonon dispersion curves is very similar to the room and low-temperature structures. The acoustic modes have a dominating peak in the frequency of 1.6 THz, which originated from the heavy Ag^+ ions, as can be observed in **Figure S26**. However, the experimental analysis does not show evidence of a new phase transition. This new phase could also be an artifact of the DFT functional or connected to the mobile nature of the Ag^+ ions.

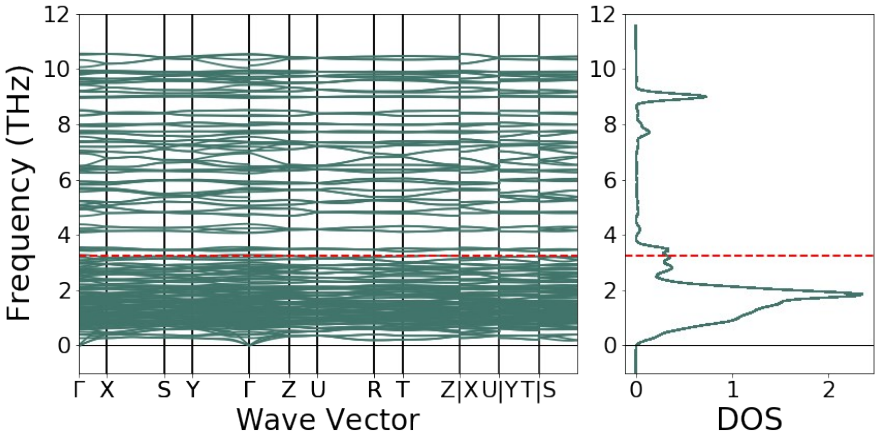

***Figure S26**. Phonon band structure together with phonon density of state for the possible phase transition of Ag_8SnS_6 argyrodites. The Debye frequency is marked in red.*

References

[1] A. A. Coelho, "TOPAS and TOPAS-Academic: an optimization program integrating computer algebra and crystallographic objects written in C++" *J. Appl. Crystallogr.* **2018**, *51*, 210–218.

[2] P. Thompson, D. E. Cox, J. B. Hastings, "Rietveld refinement of Debye–Scherrer synchrotron X-ray data from Al 2 O 3" *J. Appl. Crystallogr.* **1987**, *20*, 79–83.

[3] A. Ghata, P. L. Eckert, T. Böger, P. Garg, W. G. Zeier, "Influence of Cu+ Substitution on the Structural, Ionic, and Thermal Transport Properties of $Ag_{8-x}Cu_xGeS_6$ Argyrodites" *Chem. Mater.* **2025**, *37*, 6900–6911.

[4] T. J. Slade, V. Gvozdetskyi, J. M. Wilde, A. Kreyssig, E. Gati, L.-L. Wang, Y. Mudryk, R. A. Ribeiro, V. K. Pecharsky, J. V. Zaikina, S. L. Bud'ko, P. C. Canfield, "A Low-Temperature Structural Transition in Canfieldite, Ag_8SnS_6, Single Crystals" *Inorg. Chem.* **2021**, *60*, 19345–19355.

[5] R. Nelson, C. Ertural, J. George, V. L. Deringer, G. Hautier, R. Dronskowski, "LOBSTER : Local orbital projections, atomic charges, and chemical-bonding analysis from PROJECTOR-AUGMENTED-WAVE-BASED density-functional theory" *J. Comput. Chem.* **2020**, *41*, 1931–1940.

[6] P. C. Müller, C. Ertural, J. Hempelmann, R. Dronskowski, "Crystal Orbital Bond Index: Covalent Bond Orders in Solids" *J. Phys. Chem. C* **2021**, *125*, 7959–7970.

[7] C. Ertural, Über die elektronische Struktur funktioneller Festkörpermaterialien und ihre Beschreibung mittels lokaler Bindungsindikatoren, RWTH Aachen University, **2022**.

[8] J. Hempelmann, P. C. Müller, C. Ertural, R. Dronskowski, "The Orbital Origins of Chemical Bonding in Ge−Sb−Te Phase-Change Materials" *Angew. Chem. Int. Ed.* **2022**, *61*, e202115778.

[9] A. Yadav, P. Deshmukh, K. Roberts, N. Jisrawi, S. Valluri, "An analytic study of the Wiedemann–Franz law and the thermoelectric figure of merit" *J. Phys. Commun.* **2019**, *3*, 105001.

[10] T. Bernges, R. Hanus, B. Wankmiller, K. Imasato, S. Lin, M. Ghidiu, M. Gerlitz, M. Peterlechner, S. Graham, G. Hautier, Y. Pei, M. R. Hansen, G. Wilde, G. J. Snyder, J. George, M. T. Agne, W. G. Zeier, "Considering the Role of Ion Transport in Diffuson-

Dominated Thermal Conductivity" *Adv. Energy Mater.* **2022**, *12*, DOI 10.1002/aenm.202200717.
[11] K. Funke, R. D. Banhatti, D. Wilmer, R. Dinnebier, A. Fitch, M. Jansen, "Low-Temperature Phases of Rubidium Silver Iodide: Crystal Structures and Dynamics of the Mobile Silver Ions" *J. Phys. Chem. A* **2006**, *110*, 3010–3016.
[12] A. I. Pogodin, M. J. Filep, V. Yu. Izai, O. P. Kokhan, P. Kúš, "Crystal growth and electrical conductivity of Ag_7PS_6 and Ag_8GeS_6argyrodites" *J. Phys. Chem. Solids* **2022**, *168*, 110828.
[13] T. Bernges, R. Hanus, B. Wankmiller, K. Imasato, S. Lin, M. Ghidiu, M. Gerlitz, M. Peterlechner, S. Graham, G. Hautier, Y. Pei, M. R. Hansen, G. Wilde, G. J. Snyder, J. George, M. T. Agne, W. G. Zeier, "Considering the Role of Ion Transport in Diffuson-Dominated Thermal Conductivity" *Adv. Energy Mater.* **2022**, *12*, 2200717.
[14] J. T. S. Irvine, D. C. Sinclair, A. R. West, "Electroceramics: Characterization by Impedance Spectroscopy" *Adv. Mater.* **1990**, *2*, 132–138.
[15] W. Li, S. Lin, B. Ge, J. Yang, W. Zhang, Y. Pei, "Low Sound Velocity Contributing to the High Thermoelectric Performance of Ag8SnSe6" *Adv. Sci.* **2016**, *3*, 1600196.
[16] G. A. Slack, S. Galginaitis, "Thermal Conductivity and Phonon Scattering by Magnetic Impurities in CdTe" *Phys. Rev.* **1964**, *133*, A253–A268.
[17] G. A. Slack in *Solid State Phys.* (Eds.: H. Ehrenreich, F. Seitz, D. Turnbull), Academic Press, **1979**, pp. 1–71.
[18] G. A. Slack, "Nonmetallic crystals with high thermal conductivity" *J. Phys. Chem. Solids* **1973**, *34*, 321–335.
[19] A. M. Ganose, H. Sahasrabuddhe, M. Asta, K. Beck, T. Biswas, A. Bonkowski, J. Bustamante, X. Chen, Y. Chiang, D. C. Chrzan, J. Clary, O. A. Cohen, C. Ertural, M. C. Gallant, J. George, S. Gerits, R. E. A. Goodall, R. D. Guha, G. Hautier, M. Horton, T. J. Inizan, A. D. Kaplan, R. S. Kingsbury, M. C. Kuner, B. Li, X. Linn, M. J. McDermott, R. S. Mohanakrishnan, A. N. Naik, J. B. Neaton, S. M. Parmar, K. A. Persson, G. Petretto, T. A. R. Purcell, F. Ricci, B. Rich, J. Riebesell, G.-M. Rignanese, A. S. Rosen, M. Scheffler, J. Schmidt, J.-X. Shen, A. Sobolev, R. Sundararaman, C. Tezak, V. Trinquet, J. B. Varley, D. Vigil-Fowler, D. Wang, D. Waroquiers, M. Wen, H. Yang, H. Zheng, J. Zheng, Z. Zhu, A. Jain, "Atomate2: modular workflows for materials science" *Digit. Discov.* **2025**, *4*, 1944–1973.
[20] A. M. Ganose, H. Sahasrabuddhe, M. Asta, K. Beck, T. Biswas, A. Bonkowski, J. Bustamante, X. Chen, Y. Chiang, D. C. Chrzan, J. Clary, O. A. Cohen, C. Ertural, M. C. Gallant, J. George, S. Gerits, R. E. A. Goodall, R. D. Guha, G. Hautier, M. Horton, T. J. Inizan, A. D. Kaplan, R. S. Kingsbury, M. C. Kuner, B. Li, X. Linn, M. J. McDermott, R. S. Mohanakrishnan, A. A. Naik, J. B. Neaton, S. M. Parmar, K. A. Persson, G. Petretto, T. A. R. Purcell, F. Ricci, B. Rich, J. Riebesell, G.-M. Rignanese, A. S. Rosen, M. Scheffler, J. Schmidt, J.-X. Shen, A. Sobolev, R. Sundararaman, C. Tezak, V. Trinquet, J. B. Varley, D. Vigil-Fowler, D. Wang, D. Waroquiers, M. Wen, H. Yang, H. Zheng, J. Zheng, Z. Zhu, A. Jain, "Correction: Atomate2: modular workflows for materials science" *Digit. Discov.* **2025**, *4*, 2639–2640.
[21] W. Chen, J.-H. Pöhls, G. Hautier, D. Broberg, S. Bajaj, U. Aydemir, Z. M. Gibbs, H. Zhu, M. Asta, G. J. Snyder, B. Meredig, M. A. White, K. Persson, A. Jain, "Understanding thermoelectric properties from high-throughput calculations: trends, insights, and comparisons with experiment" *J. Mater. Chem. C* **2016**, *4*, 4414–4426.
[22] S. P. Ong, W. D. Richards, A. Jain, G. Hautier, M. Kocher, S. Cholia, D. Gunter, V. L. Chevrier, K. A. Persson, G. Ceder, "Python Materials Genomics (pymatgen): A robust, open-source python library for materials analysis" *Comput Mater Sci* **2013**, *68*, 314.
[23] D. G. Cahill, S. K. Watson, R. O. Pohl, "Lower limit to the thermal conductivity of disordered crystals" *Phys. Rev. B* **1992**, *46*, 6131–6140.

[24] M. T. Agne, R. Hanus, G. J. Snyder, "Minimum thermal conductivity in the context of diffuson-mediated thermal transport" *Energy Environ. Sci.* **2018**, *11*, 609–616.
[25] G. A. Slack, "Nonmetallic crystals with high thermal conductivity" *J. Phys. Chem. Solids* **1973**, *34*, 321–335.
[26] G. Qin, A. Huang, Y. Liu, H. Wang, Z. Qin, X. Jiang, J. Zhao, J. Hu, M. Hu, "High-throughput computational evaluation of lattice thermal conductivity using an optimized Slack model" *Mater. Adv.* **2022**, *3*, 6826–6830.
[27] M. Simoncelli, N. Marzari, F. Mauri, "Unified theory of thermal transport in crystals and glasses" *Nat. Phys.* **2019**, *15*, 809–813.
[28] Y. Xia, D. Gaines, J. He, K. Pal, Z. Li, M. G. Kanatzidis, V. Ozoliņš, C. Wolverton, "A unified understanding of minimum lattice thermal conductivity" *Proc. Natl. Acad. Sci.* **2023**, *120*, e2302541120.
[29] T. Bernges, M. Peterlechner, G. Wilde, M. T. Agne, W. G. Zeier, "Analytical model for two-channel phonon transport engineering" *Mater. Today Phys.* **2023**, *35*, 101107.